Clim Dyn
DOI 10.1007/s00382-012-1312-5

Climatic responses to the shortwave and longwave direct radiative effects of sea salt aerosol in present day and the last glacial maximum

Xu Yue · Hong Liao

Received: 20 September 2011 / Accepted: 4 February 2012

Abstract We examine the climatic responses to the shortwave (SW) and longwave (LW) direct radiative effects (RE) of sea salt aerosol in present day and the last glacial maximum (LGM) using a general circulation model with online simulation of sea salt cycle. The 30-year control simulation predicts a present-day annual emission of sea salt of 4,253 Tg and a global burden of 8.1 Tg for the particles with dry radii smaller than 10 μm. Predicted annual and global mean SW and LW REs of sea salt are, respectively, -1.06 and $+0.14$ W m^{-2} at the top of atmosphere (TOA), and -1.10 and $+0.54$ W m^{-2} at the surface. The LW warming of sea salt is found to decrease with altitude, which leads to a stronger net sea salt cooling in the upper troposphere. The changes in global mean air temperature by the present-day sea salt are simulated to be -0.55, -0.63, -0.86, and -0.91°K at the surface, 850, 500a, and 200 hPa, respectively. The emission of sea salt at the LGM is estimated to be 4,075 Tg year^{-1}. Relative to present day, the LGM sea salt emission is higher by about 18% over the tropical and subtropical oceans, and is lower by about 35% in the mid- and high-latitudes in both hemispheres because of the expansion of sea ice. As a result of the weakened LGM water cycle, the LGM annual and global mean burden of sea salt is predicted to be higher by 4% as compared to the present-day value. Compared with the climatic effect of sea salt in present day, the sea-salt-induced reductions in surface air temperature at the LGM have similar magnitude in the tropics but are weakened by about 0.18 and 0.14°K in the high latitudes of the Southern and Northern Hemispheres, respectively. We also perform a sensitivity study to explore the upper limit of the climatic effect of the LGM sea salt. We assume an across-the-board 30% increase in the glacial wind speed and consider sea salt emissions over sea ice, so that the model can reproduce the ratio of sea salt deposition between the LGM and present day in the high latitudes of the Southern Hemisphere as suggested by the ice core records. This sensitivity run predicts a global emission of sea salt of 11,941 Tg year^{-1} with a global burden of 20.9 Tg. With such a high loading, sea salt aerosol at the LGM can have a net RE of -2.28 W m^{-2} at the TOA and lead to an annual and global mean cooling of 1.27°K at the surface.

Keywords Sea salt aerosol · Radiative effect · Climatic responses · Last glacial maximum

X. Yue
Climate Change Research Center (CCRC),
Chinese Academy of Sciences (CAS), Beijing, China

X. Yue
Nansen-Zhu International Research Center,
Institute of Atmospheric Physics (IAP),
Chinese Academy of Sciences (CAS), Beijing, China

Present Address:
X. Yue
School of Engineering and Applied Sciences,
Harvard University, Cambridge, MA, USA

H. Liao (✉)
State Key Laboratory of Atmospheric Boundary Layer Physics and Atmospheric Chemistry (LAPC), Institute of Atmospheric Physics (IAP), Chinese Academy of Sciences (CAS),
P.O. Box 9804, Beijing 100029, China
e-mail: hongliao@mail.iap.ac.cn

1 Introduction

Aerosols of both anthropogenic and natural origin play important roles in the Earth's climate system. In the past few decades, substantial effort has been placed on the

Published online: 22 February 2012

assessment of the environmental and climatic impacts of anthropogenic aerosol species, including sulfate, nitrate, and carbonaceous aerosols (Forster et al. 2007). Natural aerosols, dominated by mineral dust and sea salt, are also important for understanding climate change, because of their large burdens in the troposphere and their interactions with the ancient and current climate (e.g., Mahowald et al. 2006b; Ma et al. 2008; Carslaw et al. 2010; Yue et al. 2011).

Sea salt aerosol is produced by winds over the oceans (Mulcahy et al. 2008). Parameterizations based on the wind production relationship estimate an annual global total emission of 1,000–10,000 trillion grams (Tg) of sea salt aerosol into the troposphere (Blanchard 1985). Sea salt particles are highly hygroscopic and easily grow to larger size (Tang et al. 1997; Irshad et al. 2009), leading to short residence time in the atmosphere. The suspended small sea salt particles are efficient in scattering solar energy, contributing largely to the marine aerosol optical depth (AOD) (Haywood et al. 1999). Sea salt aerosol is not absorptive of solar radiation; it causes similar direct radiative perturbations at the surface and at the top of the atmosphere (TOA). In addition, sea salt aerosol can influence the formation and lifetime of clouds by acting as cloud condensation nuclei (Kaufman et al. 2005), leading to indirect changes in the Earth's energy budget. Previous modeling studies reported that the estimated global annual mean direct and indirect shortwave (SW) radiative effects (RE) of sea salt aerosol are within the range of -0.15 to -3.5 W m^{-2} and -0.4 to -1.3 W m^{-2}, respectively (Haywood et al. 1999; Jacobson 2001; Grini et al. 2002; Takemura et al. 2002; Dobbie et al. 2003; Liao et al. 2004; Koch et al. 2006; Ayash et al. 2008; Ma et al. 2008). These solar radiative perturbations are comparable to or even larger than those of -0.8 to -3.0 W m^{-2} by mineral dust at the surface as summarized by Yue et al. (2010).

Sea salt aerosol is also important in influencing longwave radiative transfer. The experimentally retrieved values of the imaginary part of the refractive index of sea salt aerosol show large values at small wave numbers (Hess et al. 1998; Irshad et al. 2009), indicating that sea salt aerosol has an absorbing effect in the infrared wavebands. By combining a discrete ordinate radiative transfer model with observed atmospheric and aerosol profiles, Lubin et al. (2002) estimated that sea salt aerosol contributed to about 30% of the total LW REs by aerosols at the TOA over Indian Ocean. Satheesh and Lubin (2003) used the same radiative transfer model and found that the total surface SW aerosol RE was offset by 45% as a result of the LW RE of sea salt generated by moderate sea surface winds. Reddy et al. (2005a) utilized the Laboratoire de Météorologie Dynamique General Circulation Model (LMDZT GCM) and obtained an annual global mean all-sky LW RE of about 0.12 W m^{-2} at the TOA for sea salt aerosol, representing about 40% of its SW RE. Li et al. (2008) utilized a one dimensional radiative transfer model and estimated that the LW RE efficiency (RE per unit mass density) is about 20% of the SW component with the opposite sign. These studies showed the importance of the LW effect of sea salt aerosol, but did not further investigate the spatial and temporal characteristics of the LW effect on a global scale.

Geological records have shown that the concentrations of sea salt aerosol vary significantly during the glacial-interglacial cycles. Ice core records from both Antarctica and Greenland revealed two to five folds increases in sea salt aerosol concentrations during the last glacial maximum (LGM, about 21,000 years ago). Some studies attributed the high amount of sea salt to the stronger glacial wind which produced and/or transported aerosol to high latitudes (Petit et al. 1990; DeAngelis et al. 1997), while others considered that the local production from sea ice (especially frost flowers on the new sea ice) was the primary cause (Wagenbach et al. 1998; Rankin et al. 2002). All the previous modeling studies could not reproduce such increases in sea salt deposition at the LGM, even after taking into account the possible production of sea salt over sea ice (Reader and McFarlane 2003; Mahowald et al. 2006a). Sea salt aerosol is expected to contribute to the cooling at the LGM, but no studies, to our knowledge, estimated the climatic impact of sea salt aerosol at the LGM.

The purpose of this study is to quantify the climatic responses to the direct RE of sea salt aerosol, including both the SW and LW radiative effects, in both present-day and the LGM atmospheres. We pay special attention to (1) the spatial and temporal variations of sea salt LW and net (SW + LW) REs, and (2) the changes in air temperature in response to direct RE of sea salt in present day and the LGM. The descriptions of the numerical model and simulations are presented in the next section. Section 3 shows and evaluates the simulated present-day sea salt concentration and optical depth. In Sect. 4, the spatial and temporal characteristics of sea salt RE are discussed. Section 5 analyzes the climate responses to the direct REs of sea salt aerosol in present day, which are further compared to the results at the LGM in Sect. 6. In Sect. 7, we carry out several sensitivity experiments to identify major factors that can lead to increases in sea salt deposition in the high latitudes and explore the upper limit of the climatic effect of sea salt at the LGM.

2 Model and experiments

The general circulation model (GCM) IAP9L-AGCM (Zeng et al. 1989; Zhang 1990; Liang 1996; Yue and Wang

2009) is used in this study. The model has a horizontal resolution of 4° × 5° with nine vertical layers up to 10 hPa. It is coupled with a mixed-layer ocean model (Hansen et al. 1984), which utilizes a prescribed annual mean mixed-layer depth derived by Levitus et al. (2000). Yue et al. (2009) coupled the Global Transport Model of Dust (GMOD) into the GCM to simulate the transport of mineral dust aerosol, and then Yue et al. (2010) updated the radiative transfer scheme of the GCM to consider the REs of dust aerosol at both SW and LW spectra. Based on these studies, we further implement the global transport of sea salt aerosol and its REs in the GCM in this work.

2.1 Sea salt cycle

The production of sea salt aerosol is closely related to the intensity of sea surface wind. There have been many studies that parameterize the generation of sea salt particles as a function of wind speed at 10 m, such as Monahan et al. (1986), Smith et al. (1993), and Gong (2003). The Monahan's formula was found to predict reasonable mass of sea salt particles with dry radii ranging from 0.2 to 4.0 μm (Guelle et al. 2001; Gong 2003), and the parameterization by Smith et al. (1993) was found to obtain reasonable sea salt mass for particles larger than 4.0 μm (Guelle et al. 2001). For particles smaller than 0.2 μm, Gong (2003) proposed an updated parameterization to reduce the overestimation of the flux of sea salt particle number based on the work of Monahan et al. (1986). In our simulation, we assume that particles with dry radii ranging from 0.1 to 10.0 μm are representative of the climatic effect of sea salt. As a result, parameterizations from Gong (2003), Monahan et al. (1986), and Smith et al. (1993) are combined as $F_{\text{ocean}} = f\ (U_{10})$ to calculate the production of sea salt aerosol over open oceans in the GCM. U_{10} is the wind speed at 10 meters.

Production of sea salt aerosol over sea ice is possible (Wagenbach et al. 1998; Rankin et al. 2002) but quite uncertain (Reader and McFarlane 2003; Mahowald et al. 2006a). In this study, we propose three cases to take into account the uncertainties. First, no sea salt is produced over sea ice ($F_{\text{seaice}} = 0$, hereafter referred to as ICE00 scheme). Second, sea salt is produced over sea ice under the same conditions as those over open water but with half amount [$F_{\text{seaice}} = f\ (U_{10})/2$, referred to as ICE05 scheme]. Third, sea salt is produced over sea ice only when surface wind speed is larger than an arbitrary threshold 5 m s^{-1} [$F_{\text{seaice}} = f\ (U_{10} - 5)$, referred to as ICET scheme]; the production rate is dependent on $|U_0 - 5|$ and hence smaller than that over the open oceans.

Deposition schemes for sea salt aerosol are similar to the treatments for mineral dust in the GCM (Yue et al. 2009). Dry deposition of particles is dependent on both the gravitational settling and turbulent mixing at the lowest model level. At the upper levels, only the gravitational settlement is considered. Wet deposition efficiency is determined by the precipitation rate and the size-dependent empirical constants, as described by Yue et al. (2009).

We simulate six size bins of sea salt, with dry radii of 0.1–0.2, 0.2–0.5, 0.5–1.0, 1.0–2.0, 2.0–5.0, and 5.0–10.0 μm, respectively. Each bin is transported independently; size changes by breaking or coagulation among different bins are not allowed. We consider the hygroscopic growth of the sea salt particles using the empirical formula proposed by Gerber (1985), which changes the gravitational settling velocity (dry deposition) by altering the wet radius and mass density of sea salt particles (Table 1). For example, the gravitational settling velocity for a wet sea salt particle at the relative humidity (RH) of 80% is about 2 times that for a dry particle, according to the settlement Eq. 4 in Yue et al. (2009).

2.2 Sea salt radiative effect

The original radiative transfer scheme in the GCM follows that in the NCAR Community Climate Model version 3 (CCM3, Yue and Wang 2009). In the solar spectra, the model utilizes a δ-Eddington approximation to calculate radiative fluxes at each model hour in 18 bands ranging from 0.2 to 5.0 μm (Briegleb 1992). In the thermal spectra, parameterizations for the absorptivity and emissivity of air, water vapor, ozone, and trace gases are employed in a broadband model approach (Kiehl and Briegleb 1991).

Table 1 Ratios of parameters of wet sea salt particles to those of dry particles at different relative humidity

RH (%)	0	50	70	80	90	95	98	99
r/r_d	1.00	1.57	1.79	1.97	2.35	2.92	3.91	4.91
ρ/ρ_d	1.00	0.60	0.55	0.53	0.50	0.48	0.46	0.46
V/V_d	1.00	1.47	1.76	2.03	2.73	4.06	7.09	11.07
K/K_d	1.00	2.25	2.88	3.47	5.08	8.00	13.34	21.25

Parameters includes radius (r), mass density (ρ), gravitational settling velocity (V), and specific extinction coefficient (K) at 500 nm for particles with dry radii from 0.5 to 1.0 μm. The parameters for dry particles are denoted with a subscription d

The radiation schemes are updated to consider the effects of sea salt aerosol. The AOD τ, single scattering albedo (SSA) ω, and asymmetry parameter g are calculated with the Mie theory (de Rooij and van der Stap 1984; Mishchenko et al. 1999) and are utilized in the GCM to consider the scattering of solar energy by sea salt. In the thermal bands, the exponential transmission approximation proposed by Carlson and Benjamin (1980) is employed, which is based on the thermal optical depth of aerosols (Yue et al. 2010).

The refractive indices (k_r–$i{\cdot}k_i$) of sea salt aerosol utilized in the Mie calculation are from the Optical Properties of Aerosols and Clouds (OPAC) package (Hess et al. 1998); k_r and k_i are the real and imaginary parts of the indices, respectively. k_r is around 1.5 for most wavelengths while k_i is close to zero at SW bands (Fig. 1a). The value of k_i increases with wavelength at the LW bands ($\lambda > 10$ μm), indicating strong absorption of the aerosol. Relative to dry condition, k_r at RH of 80% is reduced due to the lower scattering capability of water coat, while k_i at RH of 80% reaches up to 0.4 at the wavelengths of 15–30 μm.

For the dry sea salt particles with column burden M_d, particle radius r_d, and mass density ρ_d, the AOD can be calculated by (Tegen et al. 1997),

$$\tau_d = \frac{3Q_d}{4r_d\rho_d} \cdot M_d \tag{1}$$

where Q_d is the extinction efficiency for spherical particles derived with Mie theory. When sea salt particles are wet, the AOD is then calculated by,

$$\tau = \frac{3Q}{4r\rho} \cdot M = \frac{3QM}{4r\rho M_d} \cdot M_d \tag{2}$$

where M, r, and ρ are the column burden, radius, and mass density of wet particles, respectively. If we define $K_d = \frac{3Q_d}{4r_d\rho_d}$ and $K = \frac{3QM}{4r\rho M_d}$ as the specific extinction coefficients, the ratio K/K_d reflects the change in sea salt AOD due to the hygroscopic growth of particles (Table 1). For example, the AOD of accumulation-mode sea salt particles at the RH of 80% is 3.5 times as large as that at the dry condition. The variation of the specific extinction coefficient K with wavelength and particle size is shown in Fig. 1b. While small particles have strong scattering effect at SW spectra, large particles are efficient in influencing LW radiation.

Figure 1c shows the derived SSA of sea salt aerosol. In the solar and near-infrared spectra ($\lambda < 2$ μm), sea salt absorbs practically no energy (SSA $\approx$ 1). However, the aerosol shows strong absorption at LW spectra; the small particles in the size bin of 0.2–0.5 μm even have SSA of nearly zero as the wavelength is larger than 10 μm. In addition, the aerosol becomes more absorptive when air humidity increases.

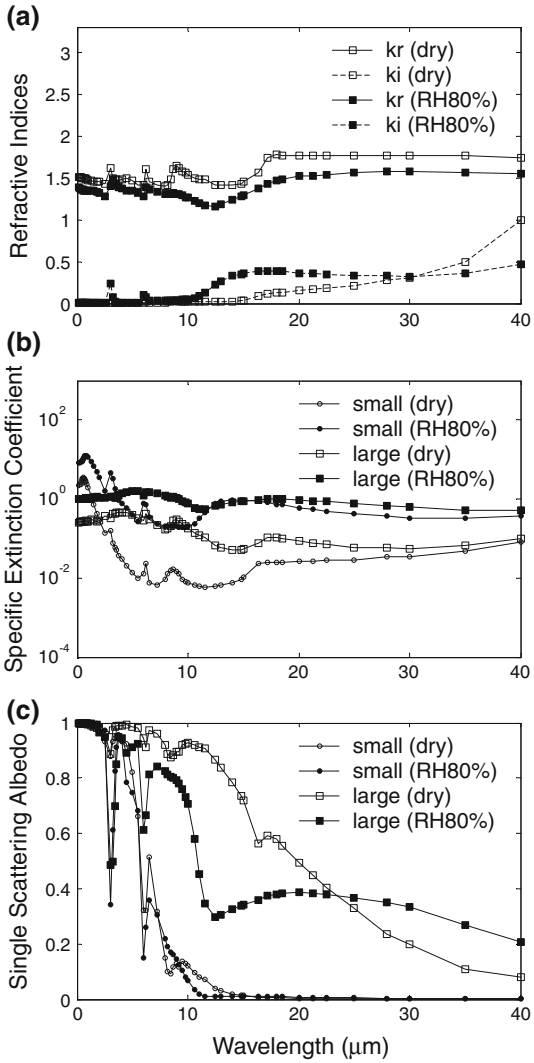

Fig. 1 Optical parameters of sea salt aerosol at different air humidity. **a** Refractive indices (k_r–$i{\cdot}k_i$); **b** specific extinction coefficient K, *unit* $m^2\ g^{-1}$; **c** SSA, unit: fraction. The dry air and wet air with 80% relative humidity are denoted as "dry" and "RH80%", respectively. Particles from the 2nd and 5th bins are, respectively, denoted as the "small" and "large" aerosols in (**b**) and (**c**). The vertical coordinate of (**b**) is logarithmic

The RE of sea salt aerosol is calculated with the "double radiation call" method as described in Woodward (2001). This method calls the radiative transfer scheme twice at every time step; one includes sea salt radiative effects and the other omits them. Only the latter call feeds the calculated sea-salt-free radiation fluxes back into the GCM to change the simulated atmospheric circulation. As a result, the meteorological fields are kept the same as those in the control run (see Sect. 2.3). The RE of sea salt aerosol is derived as the differences in the radiative fluxes between these two calls.

2.3 Numerical experiments

2.3.1 Climate simulations

We perform five climate simulations to quantify the climatic responses to the direct REs of sea salt aerosol in present day and the last glacial maximum (Table 2). Two simulations, PD_CTRL and PD_CPLD, are carried out for present day. The PD_CTRL simulates present-day sea salt aerosol online, but sea salt RE is not allowed to feed back into the GCM. The PD_CPLD has coupled sea salt-climate for present day; the suspended sea salt particles influence climate by SW and LW REs, while the perturbed meteorological fields affect sea salt cycle in turn. The differences between PD_CPLD and PD_CTRL indicate the interactive climatic effects of sea salt aerosol in present-day atmosphere. For the present-day simulations, greenhouse gases concentrations are taken from the 20C3 M scenario from the Intergovernmental panel on climate change (IPCC) fourth assessment report (AR4) database (Table 3), and the sea surface temperatures (SST) over open water are calculated with the present-day Q-flux ocean.

Similarly, we perform simulations LGM_CTRL and LGM_CPLD to understand the climatic effect of sea salt at the LGM (Table 2). The CO_2 concentration at the LGM is set to 185 ppm (Table 3), which is about half of the present-day level. The LGM continental ice sheet, topography, and coastline are implemented into IAP9L-AGCM using the datasets from Peltier (2004), with the similar treatment to that in Yue et al. (2011). The land cover at the LGM is taken from the simulation performed by Jiang (2008), who used the same version of the GCM and obtained the LGM land surface by running the equilibrium vegetation model BIOME3 (Haxeltine and Prentice 1996) driven by the climatological differences between the LGM and the present day. It was found that the area of arid and semiarid regions expands by 82% at the LGM relative to present day, as a result of the low air temperature, precipitation, atmospheric CO_2 concentration, and exposure of coastlines from decreased sea level (Jiang 2008). The LGM SSTs over open water are calculated using the LGM Q-flux ocean, which is obtained based on the energy balance between the predicted net atmosphere-to-ocean heat flux and the water heat content within the oceanic mixed layer from the CLIMAP (Climate: Long-range Investigation, Mapping, and Prediction) LGM SSTs (CLIMAP Project Members 1981). Following Manabe and Broccoli (1985), the depth of the mixed layer ocean at the LGM is assumed to be the same as that in present day. The ocean model does not simulate the dynamics of sea ice; it reports a new sea ice grid if the simulated SST is lower than 273.15°K. The temperature of sea ice is taken from the monthly sea ice climatology of the CLIMAP dataset (Yue et al. 2011).

We perform an additional climate simulation, LGMU 130_CPLD, for LGM (Table 2). In LGMU130_CPLD, we assume an across-the-board increase in glacial wind speed by 30% in the sea salt emission scheme, and, unlike the simulations PD_CTRL, PD_CPLD, LGM_CTRL, and LGM_CPLD that have zero sea salt emission from sea ice, this simulation accounts for sea salt generation over ice with the ICET scheme. All other parameters in the climate simulation LGMU130_CPLD are the same as those in the sensitivity

Table 2 List of climate simulations

Climate simulations	50 years of model integration with 20-year spin up
PD_CTRL	Present-day sea salt cycle
	Present-day climate without climatic effects of sea salt
	No sea salt emission over sea ice
PD_CPLD	Present-day interactive sea salt and climate
	No sea salt emission over sea ice
LGM_CTRL	LGM sea salt cycle
	LGM climate without climatic effects of sea salt
	No sea salt emission over sea ice
LGM_CPLD	LGM interactive sea salt and climate
	No sea salt emission over sea ice
LGMU130_CPLD	LGM interactive sea salt and climate
	Wind speed increases by 30% for aerosol emission
	Sea salt emission scheme of ICET over sea ice

Table 3 Concentrations of greenhouse gases for climate simulations

	Model year[c]	CO_2 (ppm)	CH_4 (ppb)	N_2O (ppb)	CFC_{11} (ppt)	CFC_{12} (ppt)
LGM[a]	−19000	185	350	200	0	0
PD[b]	1990	353	1,676	309	263	479

[a] Source: http://pmip2.lsce.ipsl.fr/design/boundary.shtml

[b] Source: http://www.mri-jma.go.jp/Dep/cl/cl4/IPCC-AR4/GHG_hist_table.html

[c] Model year is used to calculate Earth's orbital parameters with the equations from Berger (1978)

experiment LGM_U130_IT (see Sect. 2.3.2), except that the former one considers the climatic responses to the REs of sea salt.

Each climate simulation is integrated for 50 years and the averaged values of the last 30 years are considered as the model climatology and shown in Sect. 5, 6, and 7. The Student *t* test is used to calculate the statistical significance of the model results, and only the differences that exceed the 95% confidence level will be discussed.

2.3.2 *Sensitivity tests*

We perform four groups of sensitivity experiments to estimate the possible contributions of sea salt emissions from sea ice and/or changes in wind speed to the glacial sea salt deposition (Table 4). The first group of experiments (PD_U100_I00, PD_U100_I05, and PD_U100_IT) are the reference tests, which utilize present-day sea ice distribution and wind fields. The second group (PD_U120_I00, PD_U120_I05, and PD_U120_IT) also uses present-day sea ice distribution, but the present-day wind fields are increased by 20% when calculating sea salt emissions. The third group (LGM_U100_I00, LGM_U100_I05, and LGM_U100_IT) considers the LGM sea ice distribution and LGM wind fields. The last group (LGM_U130_I00, LGM_U130_I05, and LGM_U130_IT) has the LGM sea ice distribution but assumes a 30% increase in the LGM wind speed for sea salt emission. In each group, we perform three separate experiments with different aerosol emission schemes over sea ice (ICE00, ICE05, or ICET). Each sensitivity experiment is integrated for 15 years with the first 5 years as the spin-up. We discuss their results in Sect. 7.

Table 4 List of sensitivity simulations

Simulations	15 years of model integration with 5-year spin up
PD_U100_I00	Present-day wind speed and sea ice distribution with ICE00 scheme, same as PD_CTRL
PD_U100_I05	Present-day wind speed and sea ice distribution with ICE05 scheme
PD_U100_IT	Present-day wind speed and sea ice distribution with ICET scheme
PD_U120_I00	Same as PD_U100_I00 but wind speed increased by 20%
PD_U120_I05	Same as PD_U100_I05 but wind speed increased by 20%
PD_U120_IT	Same as PD_U100_IT but wind speed increased by 20%
LGM_U100_I00	LGM wind speed and sea ice distribution with ICE00 scheme, same as LGM_CTRL
LGM_U100_I05	LGM wind speed and sea ice distribution with ICE05 scheme
LGM_U100_IT	LGM wind speed and sea ice distribution with ICET scheme
LGM_U130_I00	Same as LGM_U100_I00 but wind speed increased by 30%
LGM_U130_I05	Same as LGM_U100_I05 but wind speed increased by 30%
LGM_U130_IT	Same as LGM_U100_IT but wind speed increased by 30%

For the cases with increased wind speed, the increased wind velocities are used for emissions of sea salt only

3 Simulated present-day sea salt cycle

3.1 Sea salt budget

The predicted present-day sea salt cycle in PD_CTRL is examined and evaluated in this section. Figure 2 shows the simulated seasonal mean emissions of sea salt. Sea salt production is always more active in the winter hemisphere. In December–January–February (DJF) (Fig. 2a), the strong winds from the active Aleutian Low and the Azores High lead to large sea salt production over the North Pacific and the North Atlantic. In June–July–August (JJA) (Fig. 2c), sea salt production becomes quite active in the middle latitudes of the southern hemisphere (SH), due to the intensified circumpolar westerlies there in this season. Large emissions of sea salt are predicted over the Arabian Sea as a result of the strengthened Indian summer monsoon. On a global scale, the simulated total sea salt emission is 4,253 Tg year^{-1} with small seasonal variation. The simulated seasonality of sea salt production is consistent with that in previous studies (e.g., Erickson et al. 1986; Gong et al. 1997; Grini et al. 2002).

The simulated sea salt budget for different size bins is shown in Table 5. Sea salt emission is predicted to increase with particle size; the largest particles ($r \geq 5.0$ μm) contribute to 62.3% of the total emission. Wet deposition removes over 94% of the sub-micron particles, and dry deposition accounts for 68% of the total deposition for super-micron particles. On an annual and global mean basis, the simulated sea salt burden is 8.1 Tg. The smallest sea salt particles with dry radii of 0.1–0.2 μm have the longest lifetime of 3.3 days, and the largest particles with dry radii of 5–10 μm deposit within a few hours. Averaged over all the size bins, the simulated lifetime of suspended sea salt particles is 0.7 days.

The simulated present-day sea salt budget is compared with previous model results in Table 6. Most models simulated the sea salt particles with dry radii smaller than 10.0 μm and obtained annual global emissions of 1,000–12,000 Tg year^{-1}. The simulated global burdens of sea salt in different models ranged from 3.8 to 25.7 Tg. Our simulated sea salt burden is within the range of previous studies.

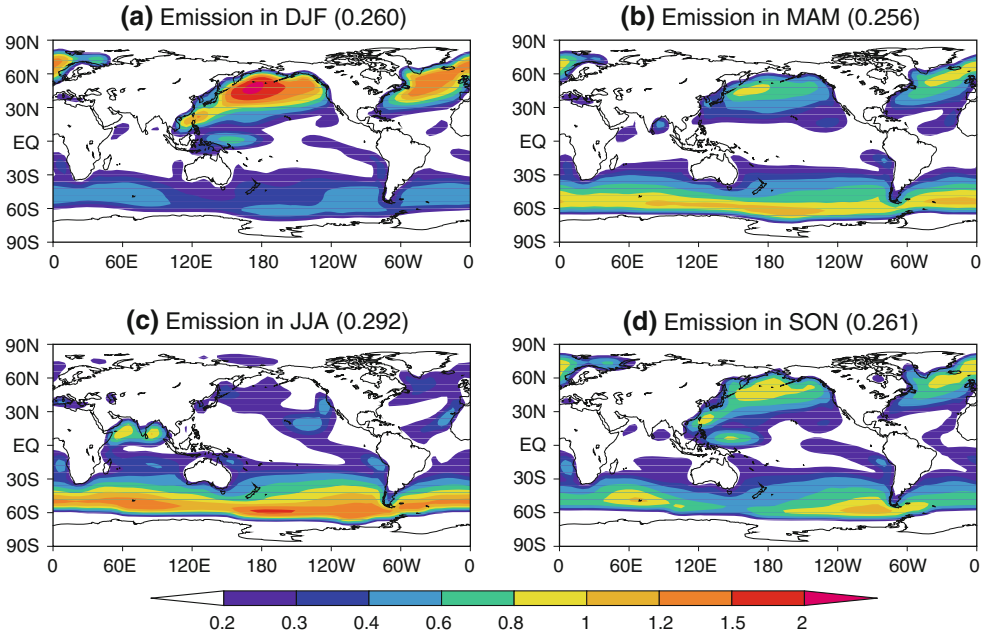

Fig. 2 Simulated sea salt emission in **a** DJF; **b** MAM; **c** JJA; **d** SON. The global averages are shown in the *parentheses*. *Unit* μg m^{-2} s^{-1}

Table 5 Simulated global sea salt budget in present day (PD_CTRL)

Dry radius (μm)	Production (Tg $year^{-1}$)	Dry deposition (Tg $year^{-1}$)	Wet deposition (Tg $year^{-1}$)	Burden (Tg)	Lifetime (days)
0.1–0.2	5	0	5	0.0	3.3
0.2–0.5	44	1	44	0.4	3.2
0.5–1.0	213	13	199	1.7	2.9
1.0–2.0	545	109	436	2.8	1.9
2.0–5.0	794	448	346	1.7	0.8
5.0–10.0	2,651	2,151	499	1.5	0.2
0.1–10.0	4,253	2,722	1,529	8.1	0.7

3.2 Station-based evaluation

3.2.1 Aerosol concentrations

The simulated present-day sea salt cycle is evaluated with measurements. The observations of sea salt concentrations are from the University of Miami Ocean Aerosol Network (Galloway et al. 1993; Prospero 1996). Figure 3 shows the distribution of the sites with observations. The operation periods were different among these sites; we use multi-year average for sites with measurements available. Since the collected sea salt particles are always wet, we examine the content of sodium ion (Na^+) in model evaluation. We calculate the mean bias (MB) and normalized mean bias (NMB) of concentrations using the following formulae (Liao et al. 2007),

$$\mathrm{MB} = \frac{1}{n}\sum_{i=1}^{n}(P_i - O_i) \tag{3}$$

$$\mathrm{NMB} = 100\% \times \sum_{i=1}^{n}(P_i - O_i) \Big/ \sum_{i=1}^{n} O_i \tag{4}$$

where P_i and O_i are predicted and observed values at site i, respectively. n is the total number of stations in the comparison. The MB and NMB of the predicted sea salt concentrations for the 20 sites are −0.11 μg m^{-3} and −1.9%, respectively. The linear correlation coefficient between observations and simulation is only 0.05 for 20 sites. The poor correlation is consistent with other studies (e.g., Ginoux et al. 2006; Koch et al. 2006), which may be attributed to the coarse resolution of the model, biases in simulated surface wind, and/or parameterization for sea salt emission.

Figure 4 compares the monthly mean sea salt concentrations at each site. We also show the monthly mean surface wind velocities during the same period of aerosol measurements calculated using the NCAR/NCEP reanalyses (Kalnay et al. 1996). Sites 1–6 are located in the

Table 6 The comparisons of simulated present-day sea salt budget in different studies

Studies	Dry radius (μm)	Emission (Tg year^{-1})	Burden (Tg)	Lifetime (days)
Gong et al. (1997)	0.03–8.0	11,700	N/A	N/A
Tegen et al. (1997)	2.0–16.0	5,900	11.4	0.71
Haywood et al. (1999)	N/A	N/A	3.8–18.8	N/A
Takemura et al. (2000)	0.1–10.0	3,529	5.6	0.58
Chin et al. (2002)	0.1–10.0	6,950	11.3	0.60
Grini et al. (2002)	0.02–12.5	6,500	6.1	0.34
Easter et al. (2004)	N/A	8,076	4.3	0.19
Liao et al. (2004)	0.03–64.0	6,056	6.9	0.40
Alexander et al. (2005)	0.1–10.0	5,370	5.9	0.40
Reddy et al. (2005b)	0.02–10.0	3,442	4.6	0.50
Tie et al. (2005)	0.1–10.0	N/A	13.2	N/A
Ginoux et al. (2006)	N/A	N/A	5.0	N/A
Koch et al. (2006)	0.1–4.0	1,734	5.2	1.10
Mahowald et al. (2006a)	0.1–10.0	5,990	12.0	0.76
Textor et al. (2006)[a]	N/A	6,280	6.4	0.41
Ma et al. (2008)	0.05–12.5	N/A	5.2	N/A
Bellouin et al. (2011)	N/A	N/A	25.7	N/A
Jaegle et al. (2011)	0.01–10.0	5,200	4.6	0.33
This study	0.1–10.0	4,253	8.1	0.70

[a] Median value of multi-model ensemble

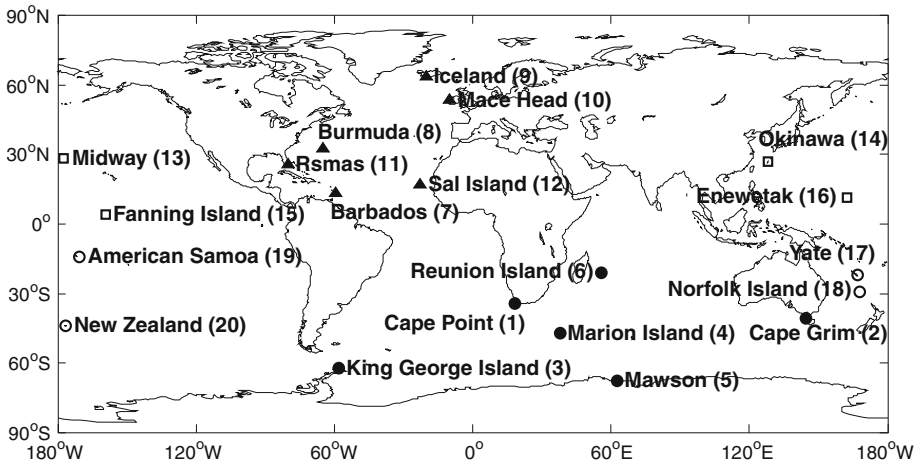

Fig. 3 Locations of 20 sites in the University of Miami Ocean Aerosol Network. *Solid circles* denote sites in the southern oceans, *triangles* denote sites in the North Atlantic, *squares* denote sites in the North Pacific, and *empty circles* denote sites in the South Pacific

southern oceans; wind speeds at these sites generally peak in JJA. At Cape Point (site 1), observed concentrations show the maximum in July and minimum in March, generally consistent with the reanalyzed seasonal variation of surface wind speed. However, simulated concentrations show small seasonal variation. At Cape Grim (site 2), both observed sea salt concentrations and reanalyzed wind speed reach maximum in August. Simulated sea salt concentrations show low bias and peak in June. King George Island (site 3) is located on the tip of the Antarctic Peninsula. Observed concentrations show high values in MAM and SON. Simulated results capture such feature although the magnitude of the springtime maximum is overestimated by about 100%. Marion Island (site 4) is located within the westerlies surrounding the Antarctic; the annual mean wind speed at this site is as high as 9.4 m s^{-1} with the maximum appears in July. However, observed sea salt concentrations are much lower than expected and exhibit small seasonal variation. Anguelova and Webster (2006) reported that other factors, such as the atmospheric stability at low level, ocean surface current velocity, duration of wind, and sea surface temperature, may also be influential on sea salt production. These factors are not considered in our sea salt generation functions, which can lead to uncertainties in

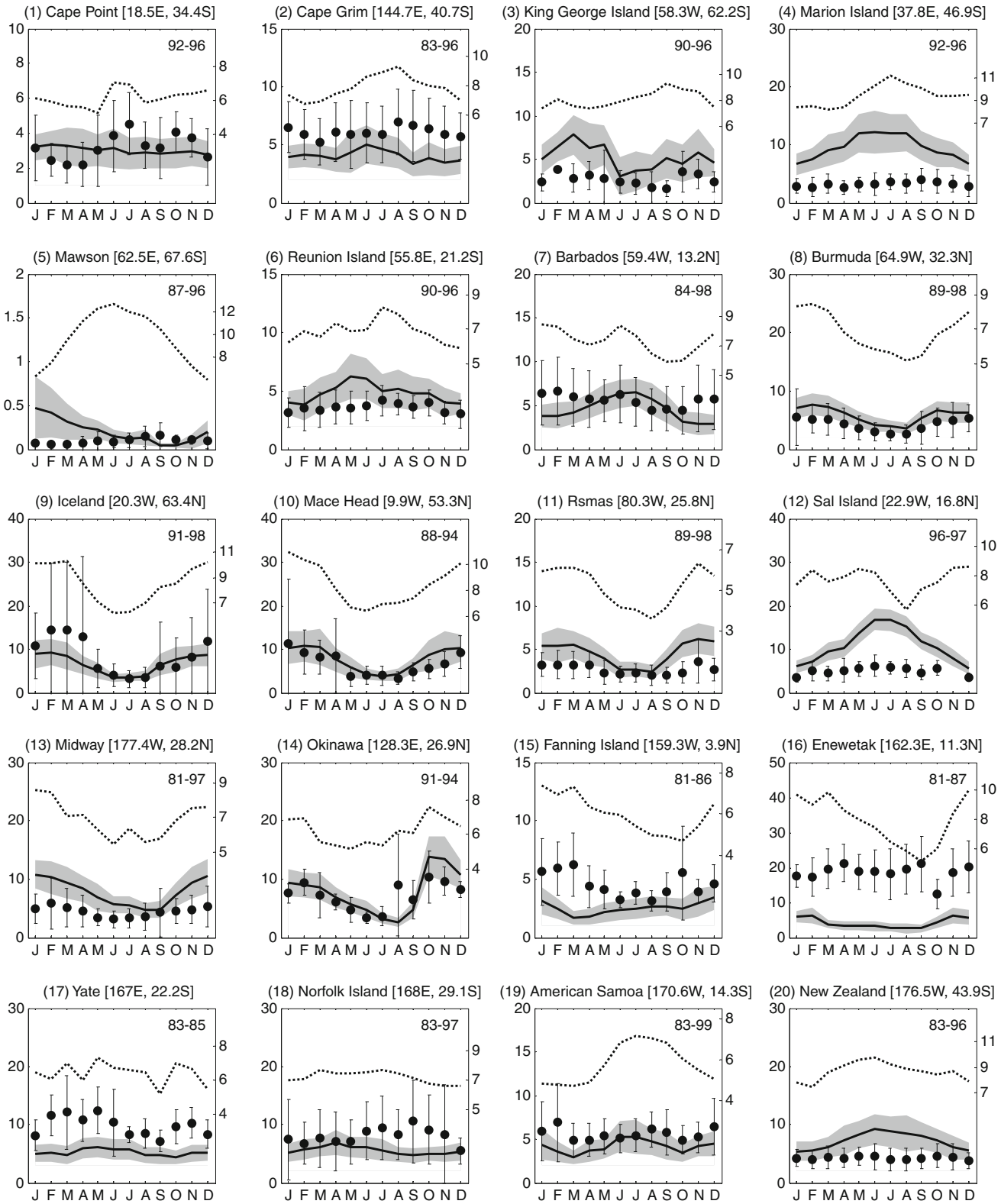

Fig. 4 Comparison of the monthly time series of Na^+ concentrations in 20 sites between observations and simulations. *Solid line* represents simulated monthly means with one standard deviation denoted by shadings. *Solid circles* are observed monthly means. *Error bars* indicate one standard deviation. The time span of available observations at each site is shown in the *upper right* hand corner of each *box*. Both the observed and predicted concentrations are scaled by the *left vertical* coordinate (*unit* μg m^{-3}). *Dotted lines* are the monthly mean surface wind speeds during the same period of aerosol measurements calculated with the NCAR/NCEP reanalyses, which are scaled by the *right vertical* coordinate (*unit* m s^{-1})

estimated sea salt emissions at some sites. Mawson (site 5) is located on the edge of Antarctica. Observed sea salt concentrations are very low, probably because the site is covered by sea ice which limits the production of sea spray. Simulated sea salt concentrations show reasonable magnitude except for the large variation during the springtime. At Renion Island (site 6), predicted sea salt concentrations are slightly higher than the observed values.

Sites 7–12 are located on the North Atlantic; simulations show good performance at these sites. At Barbados (site 7), observed sea salt concentrations peak in both JJA and DJF, which agree well with the seasonal variation of the reanalyzed surface wind speed. Predicted concentrations capture the summer maximum but have a low bias in DJF. For sites 8–11, the model reasonably reproduces the magnitude and seasonal variation of observed concentrations. The wind-dependent sea salt production function is found to be suitable for this region; strong winds generally cause large concentrations of sea salt aerosol. Sal Island (site 12) is close to the west coast of North Africa. High concentrations of sea salt aerosol are observed in JJA when surface wind speed is the minimum of the year. Our simulation captures the JJA maximum of sea salt concentration but overestimates it by about 180%.

Sites 13–16 are located over the North Pacific. Simulated aerosol concentrations match observations reasonably well and follow the seasonality of surface wind speed at Midway (site 13) and Okinawa (site 14). In Fanning Island (site 15), the abrupt increase in the observed sea salt concentration in October cannot be explained by the observed minimum local surface wind velocity in this month. The observed sea salt concentrations are very high in Enewetak (site 16), although the local wind speeds are not the strongest among the 20 sites. Simulated aerosol concentrations are much lower than the observed values at this site.

Sites 17–20 are located over the South Pacific. Yate (site 17) and Norfolk Island (site 18) are close to each other and simulations show small seasonal variations at both sites. However, observations reach peaks in MAM and SON at these two sites, respectively. Such biases may be caused by the low resolution of the GCM, which fails to resolve the seasonality of local wind. Wind speed at Samoa (site 19) shows high values in JJA, while both the observed and predicted sea salt concentrations at this site do not show large seasonal variations. At New Zealand (site 20), observed concentrations do not change significantly throughout the year, and the simulated concentrations are higher than observations during April–September.

As shown above, simulated sea salt concentrations are consistent with observations at most locations around the world, indicating the reasonableness of the simulated present-day sea salt cycle. The poor correlation between the observed concentrations and the surface wind velocities at some sites [e.g., Marion Island (site 4), Sal Island (site 12), Enewetak (site 16), and American Samoa (site 19)] indicates the requirement of more complicated parameterizations for sea salt production in future studies.

3.2.2 *Aerosol optical depth*

The predicted AODs of sea salt at 500 nm are compared with observations at eight ocean sites from AERONET (AErosol RObotic NETwork) (Holben et al. 1998) in Fig. 5. The average of observed AODs at these sites is 0.08, higher than the average of 0.06 simulated for the same sites, because the former includes the contribution from other aerosol species. At Crozet Island (site 2), modeled AODs show opposite seasonality as compared to the measurements, which may be attributed to the incorrect seasonality of the simulated wind speed in the GCM. The simulation does not capture the spring peak of AOD at Midway Island (site 4) and Coconut Island (site 5), which is probably caused by the transpacific transport of Asian dust and/or pollutants in this season. Except for these biases, simulations agree reasonably well with observations at most sites. On an annual and global basis, the simulated AOD of sea salt is 0.051 at 500 nm. This value is within the range of 0.007–0.055 estimated by previous studies (Tegen et al. 1997; Chin et al. 2002; Liao et al. 2004; Reddy et al. 2005b; Tie et al. 2005; Ginoux et al. 2006; Koch et al. 2006; Mahowald et al. 2006a; Myhre et al. 2007; Bellouin et al. 2011), most of which calculated AOD at 550 nm.

4 Radiative effect of sea salt aerosol in present day

The predicted all-sky REs of sea salt in both SW and LW spectra are shown in Fig. 6. The SW REs are negative at both the TOA (Fig. 6a) and the surface (Fig. 6b) with similar magnitude and spatial pattern. Strong SW REs are predicted around 60°S and over the tropical oceans, such as the Atlantic, the North Indian Ocean, and the East Pacific. Although aerosol concentrations are smaller in the tropics than in the mid- and high-latitudes, the stronger local solar insolation leads to similar magnitude of SW RE by sea salt in the low latitudes compared with that in the high latitudes. On an annual and global mean basis, the simulated SW REs are -1.06 W m^{-2} at the TOA and -1.10 W m^{-2} at the surface. The LW REs of sea salt are always positive (Fig. 6c and d). Because a large fraction of sea salt mass is in the lower troposphere, the LW RE is much larger at the surface than at the TOA. At the surface, the maximum LW RE is found in the mid- and high-latitudes of both hemispheres, consistent with the locations of maximum sea salt

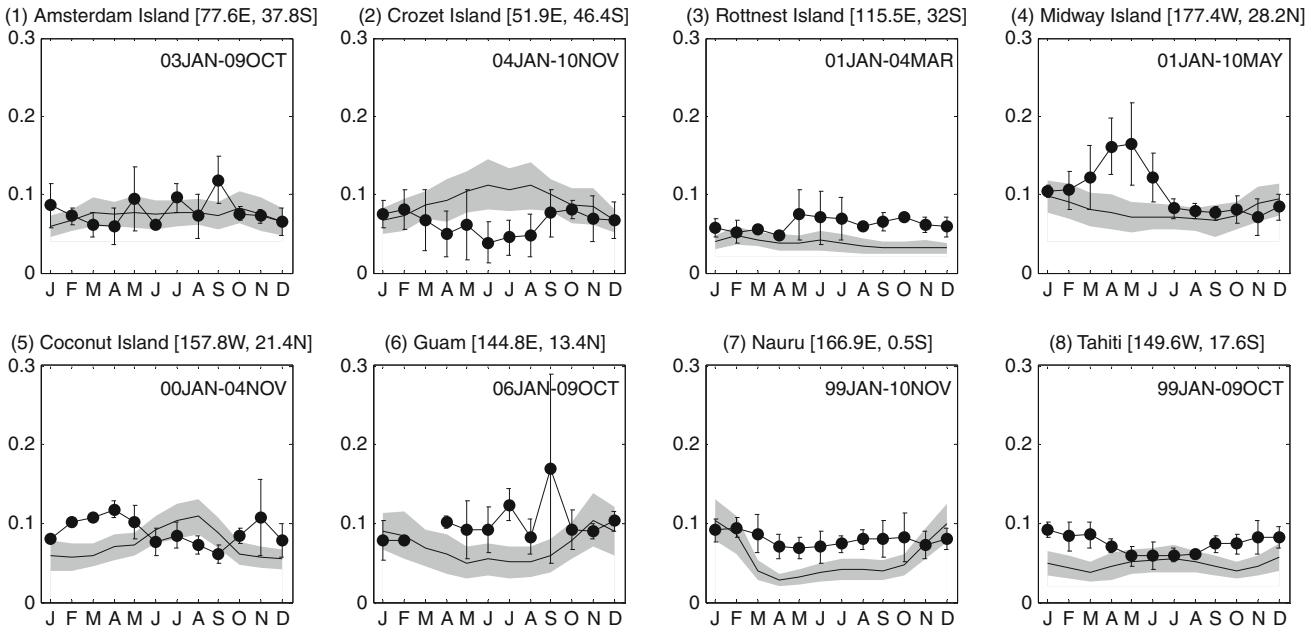

Fig. 5 Comparison of simulated aerosol optical depths at 500 nm (*dark lines* with *grey shades*) and observed AODs from AERONET (*dark solid circles* with *error bars*). The time span of available observations at each AERONET site is shown in the *top right corner* of each panel

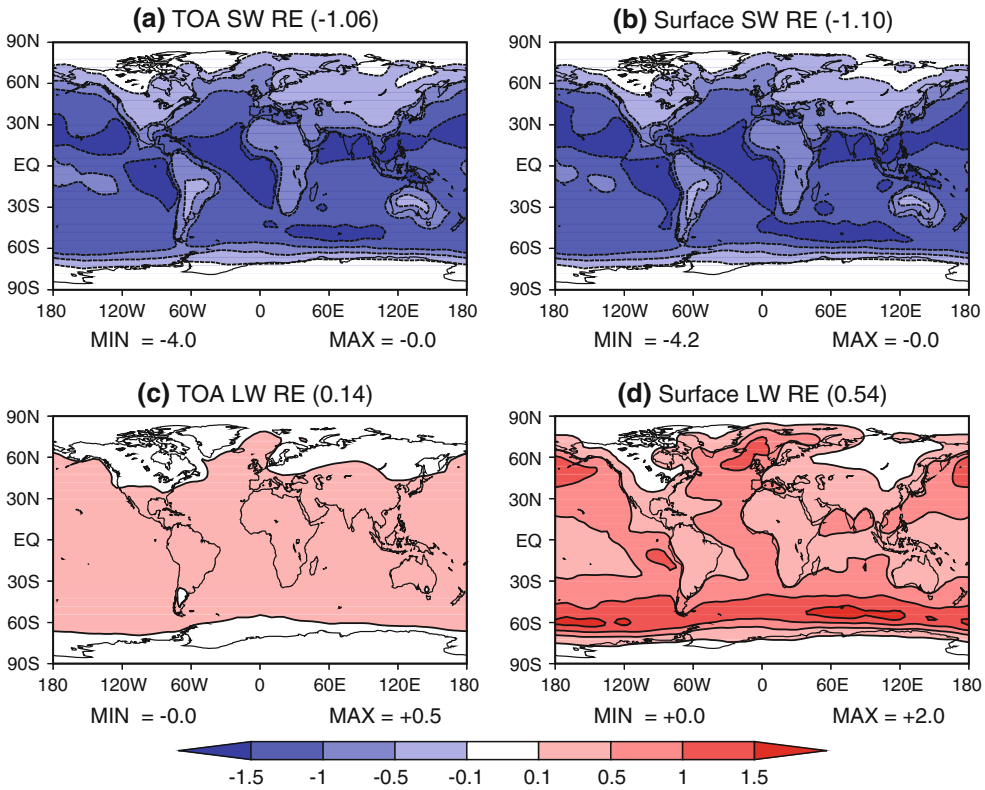

Fig. 6 Simulated annual mean all-sky RE of sea salt aerosol. **a** SW RE at TOA; **b** SW RE at surface; **c** LW RE at TOA; **d** LW RE at surface. The global averages are shown in the *parentheses*. *Positive values* indicate increases of *downward* radiation. *Unit* W m^{-2}

concentrations. The predicted global and annual mean LW REs are +0.14 and +0.54 W m^{-2} at the TOA and the surface, respectively.

The predicted present-day sea salt RE is compared with previous model estimates in Table 7. Globally, the estimated all-sky SW REs of sea salt from different studies range from −0.30 to −1.10 W m^{-2}. Our TOA all-sky SW RE of −1.06 W m^{-2} and clear-sky SW RE of −1.97 W m^{-2} are close to the values reported in Grini et al. (2002). We also compare simulated SW REs with measurement-based

Table 7 Inter-model comparisons of simulated SW RE of present-day sea salt

Studies	TOA SW RE (W m^{-2})	
	All sky	Clear sky
Haywood et al. (1999)	N/A	−1.10 to −3.50
Jacobson (2001)	−0.54	−1.10
Grini et al. (2002)	−1.10	−2.20
Takemura et al. (2002)	−0.31	−0.59
Dobbie et al. (2003)	N/A	−0.15
Liao et al. (2004)	−0.56	N/A
Reddy et al. (2005a)	−0.30	−0.63
Koch et al. (2006)	−1.10	N/A
Ayash et al. (2008)	−0.65	−1.50
Ma et al. (2008)	−0.60	−1.52
This study	−1.06	−1.97

Table 8 Measurement-based estimates of the clear-sky SW radiative efficiency (W m^{-2} τ_{aer}^{-1}) at the TOA in southern oceans (30°–60°S, 180°W–180°E)

References	Period	Data[a]	Efficiency
Christopher and Zhang (2002)[b]	September, 2000	MODIS, CERES	−44.4
Yu et al. (2004)	2000–2001	MODIS	−47.9
Loeb and Manalo-Smith (2005)	2000–2001	MODIS, CERES	−39.6
Remer and Kaufman (2006)	2003–2004	MODIS	−55.0
Myhre et al. (2007)	1996–1997	POLDER	−50 to −60
Zhao et al. (2008)	2001	MODIS, CERES	−44.6
Myhre et al. (2009)	2004	MODIS[c]	−62.4
Myhre et al. (2009)	2004	MODIS, CERES[d]	−41.7
Myhre et al. (2009)	2004	MODIS, CERES[e]	−48.2
This study	30-year average	Simulation	−36.4

[a] All the data are satellite retrievals, including radiative fluxes from the Clouds and the Earth's Radiant Energy System (CERES), aerosol optical properties from Moderate Resolution Imaging Spectroradiometer (MODIS) or Polarization and Directionality of the Earth's Reflectance (POLDER)

[b] For oceans over (20°–40°S, 100°–120°W) where sea salt dominates local AOD

[c] Followed the approach in Remer and Kaufman (2006)

[d] Followed the approach in Christopher and Zhang (2002)

[e] Followed the approach in Loeb and Manalo-Smith (2005)

estimates over the southern oceans (30°–60°S, 180°W–180°E) where sea salt has a dominant contribution to AOD. Since AODs estimated in different studies had uncertainties, the measurement-based radiative efficiencies (RE per unit AOD) are summarized and compared with our model result in Table 8. Most of the studies listed in Table 8 used AODs from Moderate Resolution Imaging Spectroradiometer (MODIS) and obtained SW REs using one of the following two approaches. The first approach obtained clear-sky SW RE by examining the differences in the instantaneous radiative fluxes measured by the Clouds and the Earth's Radiant Energy System (CERES) for cases with and without aerosols (Christopher and Zhang 2002; Loeb and Manalo-Smith 2005; Zhao et al. 2008). The second approach calculated aerosol RE with radiative transfer models using measured parameters (e.g., AOD, single scattering albedo, asymmetry factor, and surface albedo) as inputs (Yu et al. 2004; Remer and Kaufman 2006; Myhre et al. 2007). Estimated radiative efficiencies from these studies were within the range of −39.6 to −62.4 W m^{-2} τ_{aer}^{-1} with a median value of −47.9 W m^{-2} τ_{aer}^{-1}. Our simulation gives an efficiency of −36.4 W m^{-2} τ_{aer}^{-1}, which is lower than observed values by 8–42%.

Few previous studies have reported the LW RE of sea salt aerosol. Our TOA LW RE of +0.14 W m^{-2} is close to the +0.12 W m^{-2} obtained by Reddy et al. (2005a). Lubin et al. (2002) estimated that the TOA LW RE of aerosols over the Indian Ocean (mainly composed of sea salt aerosol) is about 20% of that at the surface. Our results show a similar ratio as indicated by Fig. 6.

Predicted RE of sea salt aerosol exhibits distinct seasonal variations. Fig. 7 shows the net RE of sea salt in DJF (Figs. 7a and b) and JJA (Figs. 7c, d). In DJF, the maximum sea salt concentrations are predicted over the mid- and high-latitudes of the northern hemisphere (NH). Because the incident solar radiation is small in the NH in DJF, the SW RE in the NH is simulated to be small at the surface. As a result, the positive LW RE dominates at the surface, resulting in a net warming over the northern mid- and high-latitudes where high sea salt concentrations are simulated (Fig. 7b). At the TOA, the LW RE of sea salt is much smaller than that at the surface; therefore a small proportion of SW RE is offset by LW component (Fig. 7a). The simulated global mean net REs in DJF are −0.90 W m^{-2} at the TOA and −0.56 W m^{-2} at the surface. The pattern of the net surface RE in JJA is opposite to that in DJF, with the positive REs predicted around 60°S in JJA (Fig. 7d). On a global mean basis, the net REs in JJA are predicted to be −0.91 W m^{-2} at the TOA and −0.54 W m^{-2} at the surface.

The simulated REs for particles in different size bins are shown in Table 9. We use radiative effect efficiency (REE) to denote the RE per unit mass. The particles with dry radii between 0.5 and 1.0 μm contribute to about 40% of the total SW RE at both the TOA and the surface. As expected, the larger the size, the smaller the values of SW REE. Accounting for sea salt in all size bins, the SW REEs are −0.13 W m^{-2} Tg^{-1} at the TOA and −0.14 W m^{-2} Tg^{-1}

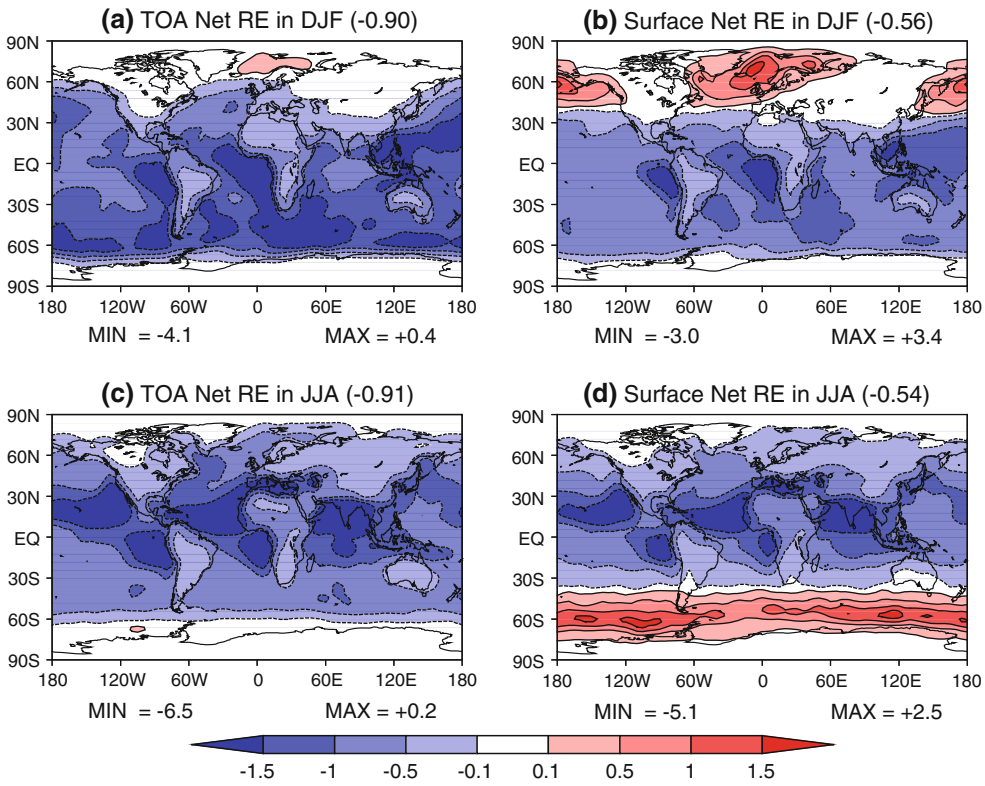

Fig. 7 Simulated all-sky net RE of sea salt aerosol in different seasons. **a** TOA net RE in DJF; **b** Surface net RE in DJF; **c** TOA net RE in JJA; **d** Surface net RE in JJA. The global averages are shown in the *parentheses. Positive values* indicate increases of *downward* radiation. *Unit* W m^{-2}

Table 9 Simulated annual global mean all-sky REs of present-day sea salt in different size bins (*unit* W m^{-2})

Dry radius (μm)	TOA			Surface		
	SW	LW	Net	SW	LW	Net
0.1–0.2	−0.04 (−0.79)	+0.00 (+0.05)	−0.04 (−0.74)	−0.04 (−0.81)	+0.00 (+0.07)	−0.04 (−0.74)
0.2–0.5	−0.21 (−0.54)	+0.02 (+0.05)	−0.19 (−0.49)	−0.21 (−0.55)	+0.03 (+0.07)	−0.18 (−0.47)
0.5–1.0	−0.44 (−0.26)	+0.06 (+0.03)	−0.39 (−0.23)	−0.46 (−0.27)	+0.13 (+0.08)	−0.32 (−0.19)
1.0–2.0	−0.30 (−0.11)	+0.05 (+0.02)	−0.25 (−0.09)	−0.32 (−0.11)	+0.20 (+0.07)	−0.11 (−0.04)
2.0–5.0	−0.07 (−0.04)	+0.01 (+0.01)	−0.06 (−0.03)	−0.08 (−0.04)	+0.12 (+0.07)	+0.04 (+0.02)
5.0–10.0	−0.02 (−0.01)	+0.00 (+0.00)	−0.02 (−0.01)	−0.02 (−0.02)	+0.07 (+0.05)	+0.05 (+0.03)
0.1–10.0	−1.06 (−0.13)	+0.14 (+0.02)	−0.92 (−0.11)	−1.10 (−0.14)	+0.54 (+0.07)	−0.56 (−0.07)

The radiative effect efficiencies (REEs) are shown in the parentheses (*unit* W m^{-2} Tg^{-1}). Positive values indicate increases of downward radiation

at the surface. For LW RE, the largest contribution to the total TOA or surface LW RE is from particles in the size range of 0.5–2.0 μm. At the TOA, smaller particles have larger LW REEs. At the surface, particles from different size bins have about the same LW REEs.

5 Climatic responses to sea salt RE in present day

In this section, we investigate climatic responses to present-day sea salt RE by examining the differences in meteorological parameters between PD_CTRL and PD_CPLD.

5.1 Air temperature

The predicted temperature responses to present-day RE of sea salt are shown in Fig. 8 for different vertical layers. Sea salt aerosol is predicted to lead to a cooling globally, which is attributed to its global mean negative net REs (Fig. 7). The surface air temperature (SAT) exhibits the largest reductions over the tropical oceans (Fig. 8a) and relatively smaller cooling in the mid- and high-latitudes of both hemispheres, because the surface LW warming partly offsets the SW cooling, especially in high latitudes where the SW RE is small in winter. On an annual and global

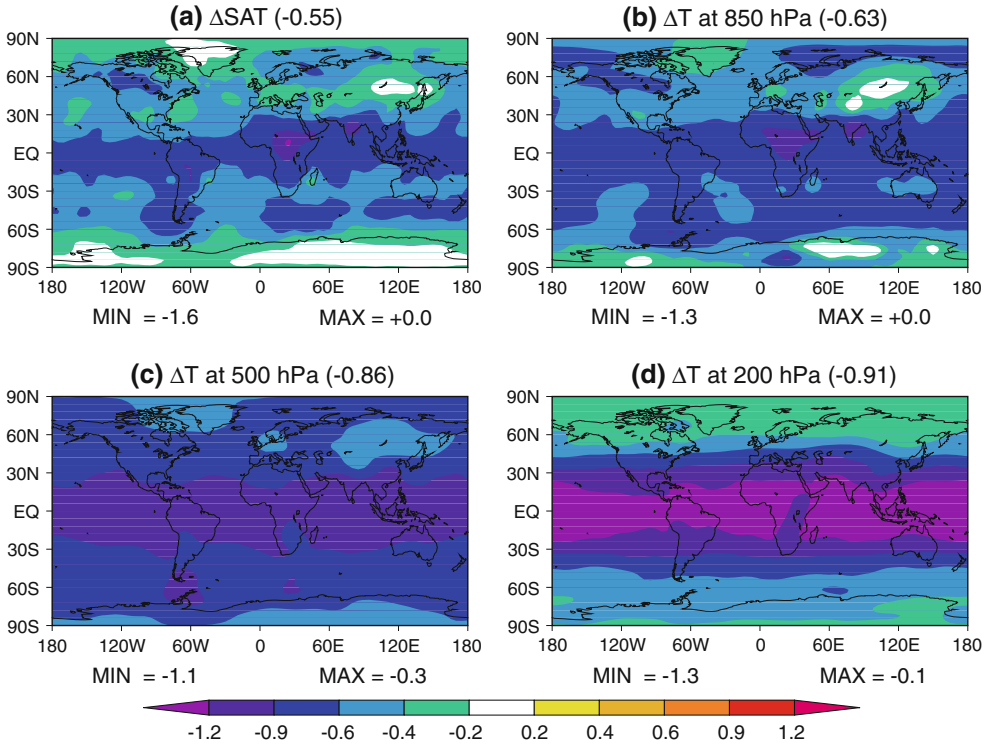

Fig. 8 Simulated annual mean changes in air temperature at **a** surface; **b** 850 hPa; **c** 500 hPa; and **d** 200 hPa in response to sea salt aerosol at present day (PD_CPLD–PD_CTRL). Results from the significance test are not shown in this figure because at least 95% of the grid cells pass the 95% confidence level. The global averages are shown in the *parentheses*. *Unit* K

mean basis, sea salt is predicted to lead to a cooling of 0.55°K in SAT.

The cooling induced by sea salt increases with altitude, as a result of the smaller LW REs at higher layers. At 850 hPa, the cooling over the mid- and high-latitudes of both hemispheres is strengthened, leading to a global mean change in air temperature of −0.63°K (Fig. 8b). At 500 hPa, the global mean air temperature is reduced by 0.86°K, with maximum reductions in air temperature found over the tropical oceans (Fig. 8c). The cooling is the strongest at 200 hPa (Fig. 8d); a widespread cooling exceeding −1.0°K is predicted over 30°S–30°N.

5.2 Surface energy balance

Figure 9a shows the changes in latent heat flux in response to sea salt RE. Large decreases in the upward transport of latent heat are predicted over the tropical oceans. This can be explained by sea-salt-induced reductions in SST (not shown), which inhibit evaporation over the oceans. Over central Africa, latent heat fluxes are predicted to increase, because of the predicted local increases in precipitation (Fig. 9d). On a global scale, the annual mean upward latent heat flux decreases by 1.17 W m^{-2} (1.7%).

The changes in the sensible heat flux are shown in Fig. 9b. Over the continents, the changes in sensible heat flux are generally opposite to those in latent heat (Fig. 9a). The increased latent heat reduces ground temperature by evaporation, leading to reduced differences in temperature between ground and surface air. As a result, the surface sensible heat fluxes decrease, and vice versa. On an annual and global mean basis, the upward sensible heat flux increases by 0.30 W m^{-2} (1.4%).

5.3 Hydrological cycle

The temperature changes induced by sea salt lead to responses in hydrological cycle. Figure 9c shows the changes in surface air humidity. The widespread decreases in air temperature (Fig. 8) lead to reductions in evaporation over the oceans. In addition, the decreases in air temperature reduce the ability of atmosphere to hold water. Both effects contribute to the large decreases in air humidity at the surface and higher layers. Since water vapor is an important greenhouse gas in the troposphere, the reduction in air moisture helps to reduce air temperature ultimately. The predicted annual global mean change in surface-layer air humidity is −0.32 g kg^{-1}.

The reductions in upward latent heat flux (Fig. 9a) further reduce precipitation, especially over the oceans (Fig. 9d). However, increased precipitation is found over the tropical Atlantic, central Africa, and the Arabian Sea. Because the sea-salt-induced cooling over the tropics is stronger in the upper troposphere than in the lower layers (Fig. 8), atmospheric stability decreases and hence clouds (Figs. 9e, f) and precipitation (Fig. 9d) increase over these tropical areas. It should be noted that sea-salt-induced changes in precipitation and cloud show fewer regions that

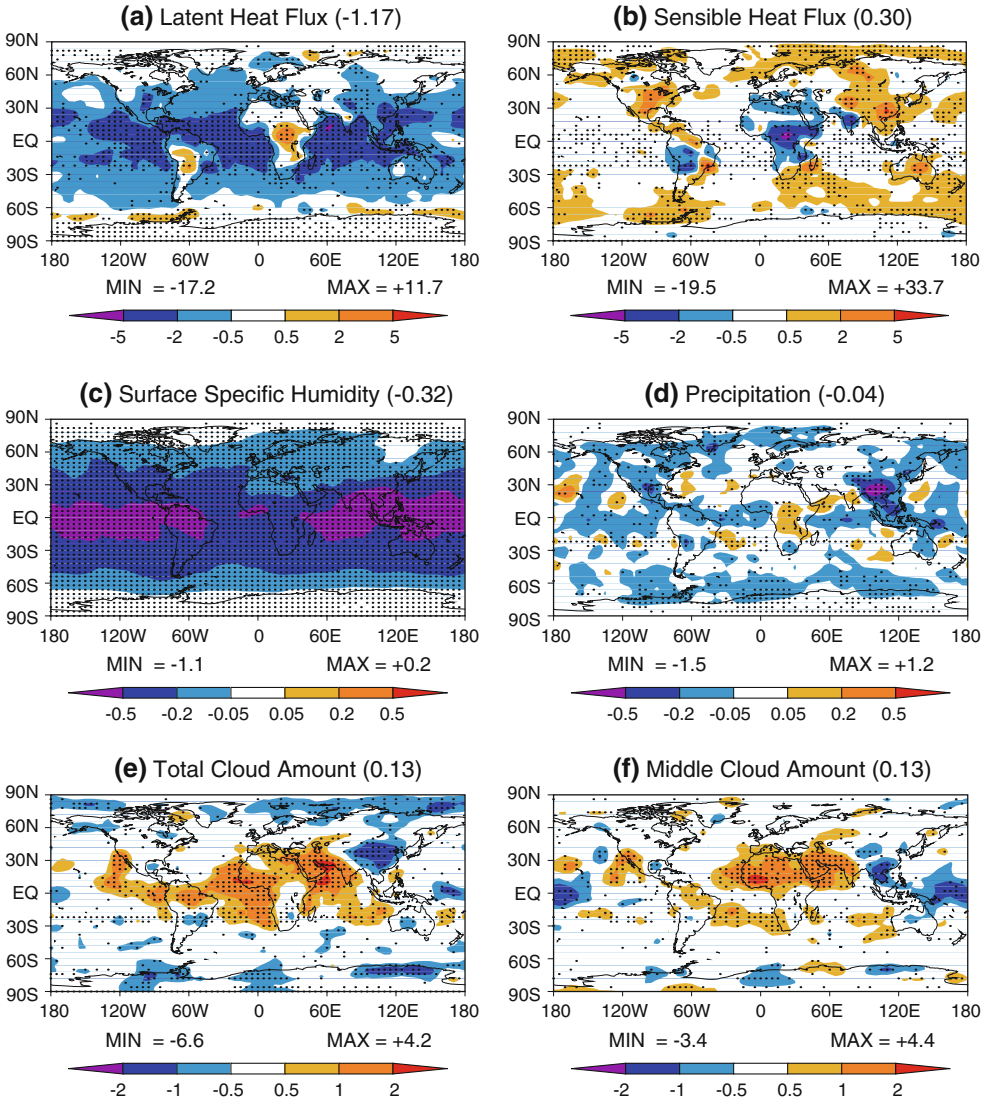

Fig. 9 Responses of meteorological fields to the RE of sea salt aerosol at present day (PD_CPLD–PD_CTRL). **a** Latent heat flux (W m^{-2}); **b** sensible heat flux (W m^{-2}); **c** surface specific humidity (g kg^{-1}); **d** precipitation (mm day^{-1}); **e** total cloud amount (%); **f** middle cloud amount (%). *Positive values* in (**a**) and (**b**) indicate increases of *upward* fluxes. The difference that passes the 95% significant level is denoted with *dot*. The globally averaged changes are indicated in *parentheses*

pass the significance test (Figs. 9d, e) as compared with the changes in temperature (Fig. 8). This is because changes in precipitation and cloud amount not only follow those in temperature, but also depend on other physical processes (e.g., water vapor supply and convection). The complicated interactions among these processes induce large internal variability in the GCM. On a global scale, annual mean precipitation is predicted to be reduced by 0.04 mm day^{-1} while both the total cloud amount and middle cloud amount increase by 0.13%.

6 Climatic responses to sea salt RE at the LGM

6.1 The LGM climate

Figure 10a shows the simulated differences in SAT between the LGM and present-day climate (LGM_CTRL–PD_CTRL). Relative to present day, a strong LGM cooling is predicted in mid- and high-latitudes in both hemispheres, mainly because of the large ice coverage and low concentrations of greenhouse gases (Jansen et al. 2007). However, a weak warming is predicted over the subtropical Pacific. Such pattern is determined by the CLIMAP LGM SSTs (CLIMAP Project Members 1981) used in our simulations; similar results are obtained by the first and second phases of Paleoclimate Modelling Intercomparison Project (PMIP1 and PMIP2) simulations (Braconnot et al. 2007). On an annual global mean basis, the predicted SAT is lowered by −4.64°K, within the estimated range of −3.3 to −4.7°K by models from PMIP1 and −3.6 to −5.7°K from PMIP2 (Braconnot et al. 2007).

The predicted changes in precipitation are shown in Fig. 10b. Compared with present day, the annual mean precipitation decreases by 0.24 mm day^{-1} globally at the LGM, although increased rainfall is predicted over the tropical oceans, especially over the tropical Pacific, as a result of the warmer-than-today SSTs in these regions as

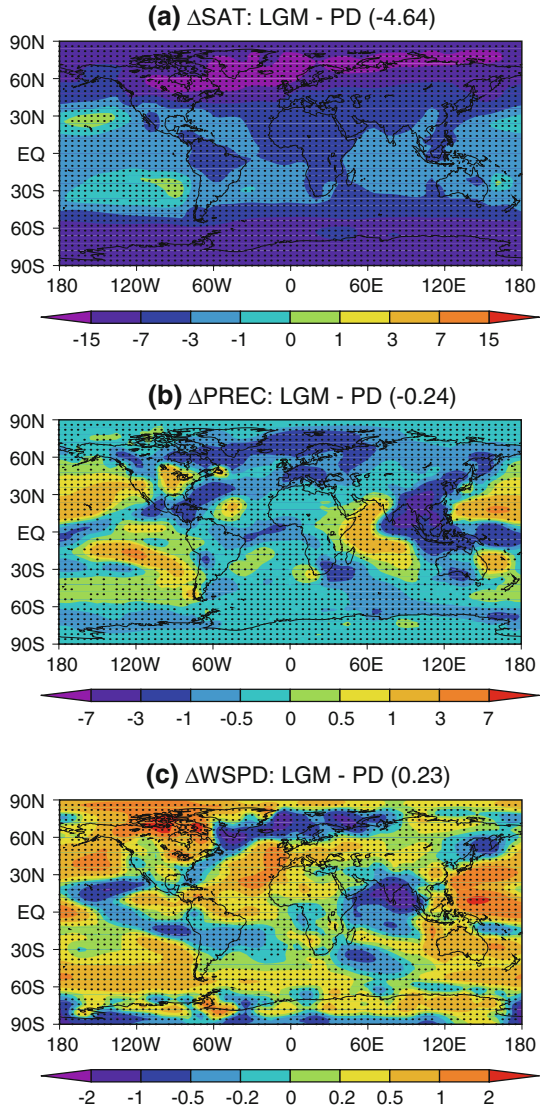

Fig. 10 Differences in the simulated **a** SAT (K), **b** precipitation (mm day^{-1}), and **c** wind speed at the lowest model level (m s^{-1}) between the LGM and present-day climate (LGM_CTRL–PD_CTRL). The difference that passes the 95% significant level is denoted with *dot*. The globally averaged differences are indicated in *parentheses*

indicated by the CLIMAP reconstructions (Jiang 2008). The largest reduction in precipitation is predicted over South Asia where heavy monsoon rainfall dominates in present day; the expansion of glacial ice sheets leads to a reduction in global sea level, leaving an increased area of desert in South Asia from the exposure of coastal land.

Another important change for the LGM climate is the wind speed (Fig. 10c). Relative to present day, an increase in the low-level wind velocity is predicted at the LGM over many regions (although decreases are also seen). The wind speed is strengthened by 5 and 6% at 50°S and 50°N, respectively. Such change could result from stronger and shifted storm tracks due to the increased temperature gradient in mid- and high-latitudes as a result of the cooler Polar Regions (Petit et al. 1981). On an annual and global mean basis, the LGM wind cubed is stronger than the present-day value by 13%.

6.2 Climatic effects of sea salt at the LGM

In response to the glacial climate, sea salt cycle shows different features at the LGM. Compared with present day, sea salt production is predicted to increase by 18% over the tropical and subtropical oceans at the LGM (Fig. 11a and Table 10), due to the stronger glacial winds (Fig. 10c). In the high latitudes in the SH and NH, sea salt emissions are simulated to be reduced by 35 and 37%, respectively (Table 10), because the expansion of sea ice during the glacial period limits the emissions of sea salt. As a result, the global total sea salt production exhibits a moderate decrease of 4% at the LGM relative to the present day, similar to the value of −5% estimated by Mahowald et al. (2006a). The ratio of the wet deposition to total deposition decreases from 36% in present day to 35.5% at the LGM, due to the reduction in global precipitation (Fig. 10b) at the glacial period. Since wet scavenging is the only efficient way to remove small particles (Table 5), the LGM annual mean global burden of the aerosol increases by 4% (Table 10) and even more for small particles with dry radius smaller than 2 μm as a result of the weakened wet deposition.

Compared with the present-day values, the LGM AOD shows large increases over the tropical and subtropical oceans and decreases in high latitudes in both hemispheres (Fig. 11b), consistent with the changes in sea salt emission (Fig. 11a). In addition, the AOD over most continents, such as Asia, Africa, Australia, and Europe, exhibits widespread increases likely due to the reduced precipitation (Fig. 10b) and hence the reduced wet deposition of sea salt at the LGM. As a result, the regionally averaged AOD increases by 13% in the tropical and subtropical areas but decreases by 33 and 15% in the high latitudes of the SH and NH, respectively, leading to a 2% increase in AOD on the global scale (Table 10).

The changes in net RE of sea salt aerosol at the LGM relative to the present day are shown in Fig. 11c and d. Over the tropical and subtropical regions, the increased AOD (Fig. 11b) leads to stronger negative REs at both the surface and the TOA. However, the decreased AOD in the high latitudes weakens the negative RE at the TOA and the positive value at the surface in both hemispheres, because the net sea salt RE in the high latitudes is negative at the TOA and positive at the surface (Fig. 7). On an annual and global mean basis, the net negative RE of the aerosol is strengthened by 0.06 W m^{-2} at the surface and 0.03 W m^{-2} at the TOA during the LGM period relative to present day.

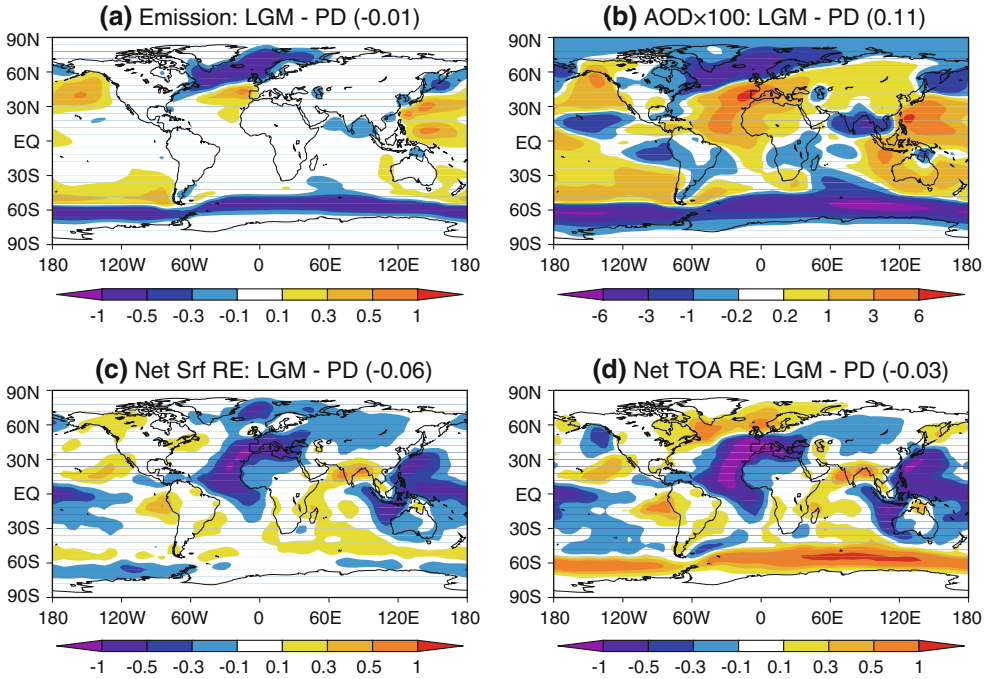

Fig. 11 Differences in the simulated **a** emission (μg m^{-2} s^{-1}), **b** AOD at 500 nm (0.01), **c** net RE at surface (W m^{-2}), and **d** net RE at the TOA (W m^{-2}) of sea salt aerosol (LGM_CTRL–PD_CTRL). The globally averaged differences are indicated in *parentheses*

Table 10 Simulated production, burden, mean AOD, and net TOA RE of sea salt, as well as the sea-salt-induced SAT responses in the present day and LGM

Climates	Production[a] (Tg $year^{-1}$)	Burden[a] (Tg)	AOD[a]	TOA net RE[a] (W m^{-2})	ΔSAT[b] (K)
Global					
PD	4,253	8.1	0.051	−0.92	−0.55
LGM	4,075	8.5	0.052	−0.96	−0.50
LGMU130	11,937	20.9	0.130	−2.28	−1.27
[45°S–45°N, 180°W–180°E]					
PD	2,514	6.3	0.055	−1.08	−0.60
LGM	2,957	7.2	0.062	−1.21	−0.61
LGMU130	7,804	16.6	0.144	−2.84	−1.53
[90°S–45°S, 180°W–180°E]					
PD	1,209	1.3	0.057	−0.78	−0.47
LGM	785	0.8	0.038	−0.47	−0.29
LGMU130	3,031	2.9	0.129	−1.31	−0.72
[45°N–90°N, 180°W–180°E]					
PD	531	0.6	0.027	−0.32	−0.41
LGM	332	0.5	0.023	−0.29	−0.27
LGMU130	1,102	1.4	0.066	−0.75	−0.63

[a] For PD and LGM, results are from simulations PD_CTRL and LGM_CTRL, respectively. For LGMU130, results are from simulation LGMU130_CPLD

[b] For PD and LGM, ΔSATs are calculated by PD_CPLD–PD_CTRL and LGM_CPLD–LGM_CTRL, respectively. For LGMU130, results are from LGMU130_CPLD–LGM_CTRL

Following the changes in RE, relative to the sea-salt-induced cooling in the present-day atmosphere, the cooling in SAT by sea salt at the LGM is stronger by 0.01°K in the tropical and subtropical latitudes (Table 10), whereas smaller by about 0.18 and 0.14°K in the high latitudes of the SH and NH, respectively. The weakened cooling in the Polar Regions can be attributed to the lower sea salt production as a result of the increased sea ice area at the LGM. On an annual and global mean basis, the surface cooling induced by sea salt at the LGM is 0.5°K, which is about the same magnitude as the sea salt cooling in the present day.

7 Sensitivity studies on climatic effects of sea salt at the LGM

7.1 Roles of wind and sea ice in simulation of the LGM sea salt emissions

Ice core record has time series of sodium concentrations during glacial and interglacial cycles, which can be used as an indicator for sea salt aerosol (Petit et al. 1999; Rothlisberger et al. 2002). Mahowald et al. (2006) assumed that the aerosol concentration in the ice core is equal to the

atmospheric deposition divided by the ice accumulation rate. By considering the ratio of precipitation between LGM and present day, they obtained ratios of 2.3, 1.9 and 4.8 for sea salt deposition between the LGM and present day, based on the data from Vostok [78°S, 107°E], Dome C [75°S, 124°E], and GRIP [73°N, 38°W]. Although we simulate an increase of 4% in global wind speed at the LGM relative to the present day (Fig. 10c), we obtain ratios of 0.24, 0.12, and 0.03 for sea salt deposition in the same locations based on the LGM_CTRL and PD_CTRL simulations. Similar underestimates in glacial deposition were also reported by other modeling studies (e.g., Reader and McFarlane 2003; Mahowald et al. 2006a).

As summarized in Table 4, we carry out several sensitivity experiments to try to identify the factors that contribute to the low bias. We examine here whether these sensitivity simulations can reproduce the ratios of aerosol deposition fluxes within the latitudinal belt of 70°–80°S as suggested in ice core data. We select the observed flux ratio of 1.9 between the LGM and present day at Dome C (75°S, 124°E) as a reference value. The ratios of deposition fluxes from the sensitivity simulations are given in Table 11. The ratios of deposition fluxes of PD_U120_I00/PD_U100_I00, PD_U120_I05/PD_U100_I05, and PD_U120_IT/PD_U100_IT are 1.30, 2.04, and 2.09 (Table 11), respectively, indicating that with the present-day sea ice distribution, the deposition fluxes increase when the wind speed is increased by 20%, even when no sea salt is allowed to emit over sea ice. For the simulations with the LGM sea ice distribution, the ratios of deposition fluxes of LGM_U100_I00/PD_U100_I00, LGM_U100_I05/PD_U100_I05, and LGM_U100_IT/PD_U100_IT are smaller than 1.0 whether with or without sea salt emissions from sea ice (Table 11), probably because the simulated increases in the regional glacial wind speed are not big enough to obtain the observed large ratios of deposition flux between the LGM and present day. Petit et al. (1981) suggested that the LGM wind velocities could be 50–80% higher than present-day values at the regions close to Antarctica. In the sensitivity tests with the LGM wind speed increased by 30%, the ratios of deposition fluxes of LGM_U130_I05/PD_U100_I05 and LGM_U130_IT/PD_U100_IT are 1.99 and 1.95 (Table 11), respectively, when we consider sea ice as a source of sea salt emissions (ICE05 or ICET). We find that the simulated deposition ratios are similar with the two different sea-ice emission schemes (ICE05 and ICET) if the same meteorological fields and sea ice distribution are applied in the simulations (Table 11), suggesting that the wind speed may be more important than the accuracy of sea-ice emission scheme in influencing simulated deposition in the polar region.

Table 11 Ratios of mean sea salt deposition flux in high latitudes in the SH (70°–80°S) between the sensitivity experiments

	Ratios
Ratios to PD_U100_I00	
PD_U120_I00	1.3
LGM_U100_I00	0.01
LGM_U130_I00	0.03
Ratios to PD_U100_I05	
PD_U120_I05	2.04
LGM_U100_I05	0.70
LGM_U130_I05	1.99
Ratios to PD_U100_IT	
PD_U120_IT	2.09
LGM_U100_IT	0.51
LGM_U130_IT	1.95

7.2 Upper limit of the climatic effect of sea salt at the LGM

Based on the results from the sensitivity experiments, we find that the simulation LGM_U130_IT can reproduce the observed ratios of sea salt deposition between the LGM and present day in the high latitudes of SH. Since the LGM_CPLD simulation has a low bias in simulation of sea salt deposition in the high latitudes of the SH, we try to estimate the upper limit of the climatic effect of sea salt at the LGM with simulation LGMU130_CPLD (Table 2).

In LGMU130_CPLD, the global aerosol production reaches 11,937 Tg year^{-1} (Fig. 12a), which is 2.9 times as large as that in LGM_CTRL (Table 10). Consistent with the changes in emission, the global burden and optical depth (Fig. 12b) of the aerosol are larger by 146% and 150%, respectively, relative to LGM_CTRL. The aerosol RE reaches -2.28 W m^{-2} globally at the TOA (Fig. 12c), which is 2.4 times the value in the LGM_CTRL simulation. In response to such a strong RE by sea salt, the global mean SAT decreases by 1.27°K at the LGM (LGMU130_CPLD–LGM_CTRL, Fig. 12d).

8 Conclusions and discussions

We present a first global modeling study that examines (1) the spatial and temporal variations of the longwave and net (shortwave plus longwave) direct radiative effects of sea salt, and (2) the climatic responses to the direct radiative effects of sea salt in present day and the LGM.

The present-day global total emission of sea salt particles with dry radii ranging from 0.1 to 10.0 μm is estimated to be 4,253 Tg year^{-1}. Predicted sea salt burden is 8.1 Tg, with an average lifetime of 0.7 day in the atmosphere. The simulated aerosol burden is within the estimates of 3.8–25.7 Tg by previous modeling studies (Table 6).The present-day sea salt is found to lead to an annual global mean SW and LW REs of -1.06 and $+0.14$ W m^{-2}, respectively, at the top of the atmosphere, and of -1.10

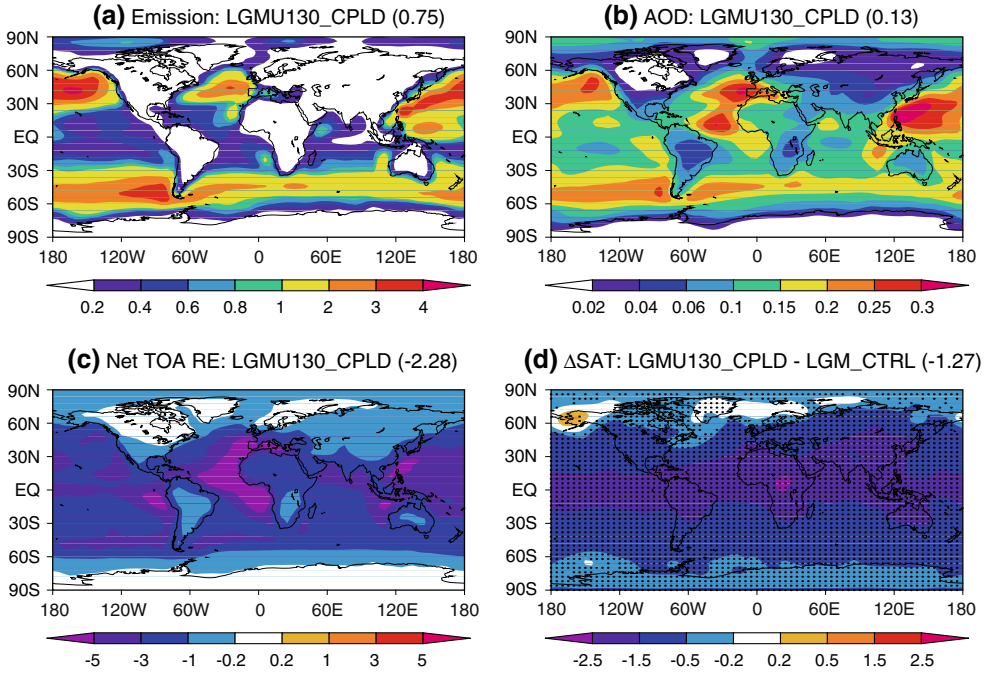

Fig. 12 Simulated **a** emission (μg m^{-2} s^{-1}), **b** AOD at 500 nm, and **c** net RE at the TOA (W m^{-2}) of sea salt aerosol in LGMU130_CPLD, and **d** the sea-salt-induced responses in SAT (K) (LGMU130_CPLD–LGM_CTRL). The difference in SAT that passes the 95% significant level is denoted with *dot*. The global averages are indicated in *parentheses*

and +0.54 W m^{-2} at the surface. Our estimated TOA LW RE is close to the value of +0.12 W m^{-2} obtained by Reddy et al. (2005a). The net RE is generally negative at the TOA, but exhibits obvious seasonal variation at the surface. Net positive REs are simulated over the mid- and high-latitudes of the winter hemisphere, because the LW RE is larger than the SW RE in those regions.

We examine the climatic responses to the net RE of sea salt. The air temperature is simulated to decrease by −0.55, −0.63, −0.86, and −0.91°K at the surface, 850, 500, and 200 hPa, respectively. The cooling at surface induced by sea salt inhibits evaporation over the oceans, leading to global reductions in latent heat flux and the upward transport of water vapor. As a result, the annual global mean precipitation decreases by 0.04 mm day^{-1}. However, regional increases in precipitation are predicted over the tropical Atlantic, central Africa, and the Arabian Sea. Because the sea-salt-induced cooling over the tropics is stronger in the upper troposphere than in the lower layers (Fig. 8), atmospheric stability decreases and hence clouds and precipitation increase over these tropical areas.

Compared with present day, the global total sea salt production is lower by 4% globally at the LGM, similar to the value of 5% estimated by Mahowald et al. (2006a). Regionally, the LGM sea salt emissions are higher by 18% over the tropical and subtropical oceans, but lower by about 35% in the mid- and high-latitudes of both hemispheres, as a result of the stronger winds and larger area of sea ice at the LGM. The annual mean global burden and optical depth of sea salt aerosol at the LGM are larger, by 4 and 2%, respectively, than the values in the present day, because of the reduced precipitation (or the wet deposition of sea salt) at the LGM. The net negative RE of sea salt at the LGM is stronger by 0.06 W m^{-2} at the surface and 0.03 W m^{-2} at the TOA as compared with the present-day values. In response to the differences in RE between LGM and the present day, the LGM sea-salt-induced cooling in SAT is larger by about 0.01°K in the tropical and subtropical latitudes, but smaller by about 0.18 and 0.14°K in the high latitudes of the SH and NH, respectively. Globally, the surface cooling induced by sea salt is 0.5°K at the LGM, which is very close to the value in the present day.

Our model does not reproduce the large increases in sea salt deposition in the high latitudes during the glacial period as indicated by ice core records. Since similar underestimates were reported by previous studies (e.g., Reader and McFarlane 2003; Mahowald et al. 2006a), we perform sensitivity simulations to try to identify the causes for such underestimation. The best estimate is obtained in the sensitivity run that has a 30% increase in LGM wind speed and has sea salt emissions over sea ice. In this sensitivity simulation, the estimated global sea salt emission is 11,937 Tg $year^{-1}$ and the global burden reaches 20.9 Tg. This high loading of aerosol leads to a net RE of −2.28 W m^{-2} at the TOA and a sea-salt-induced global mean cooling of 1.27°K at the surface at the LGM. The simulated change of −1.27°K in global mean SAT by sea salt in the sensitivity experiment is likely, considering that the simulated LGM aerosol burden of 20.9 Tg is even within the range of present-day estimates from other studies (3.8–25.7 Tg shown in Table 6). This global mean cooling of 1.27°K by the artificially increased LGM sea

salt is much stronger than the cooling of 0.55°K induced by present-day sea salt, indicating that sea salt may have a large contribution to the strong cooling in the glacial period. It should be noted that although we use ratios of sea salt deposition at the LGM to that in the present day, the ratios from ice core have large uncertainties. For example, the increases in sea salt observed in the ice cores at the LGM could be from continental sources and may not represent sea salt deposition (Bigler et al. 2006).

The indirect effects of sea salt aerosol are not considered in our simulations. Previous studies estimated that sea salt leads to an annual global mean indirect SW RE of −0.38 to −1.34 W m^{-2} (Ayash et al. 2008; Ma et al. 2008). This magnitude is comparable to our predicted direct SW RE of sea salt aerosol in the present day, which should be considered in our future studies.

Acknowledgments We thank J. M. Prospero and D. L. Savoie for their generous offer of the observed sea salt concentrations from the University of Miami Ocean Aerosol Network. We also acknowledge the two anonymous reviewers for their helpful comments. This work was supported by the CAS Strategic Priority Research Program Grant No. XDA05100503, the National Natural Science Foundation of China under grants 40825016 and 90711004, the special funding in atmospheric science GYHY20086006, and the National Basic Research Program of China (''973'' program) under grant 2010CB951901.

References

Alexander B, Savarino J, Lee CCW, Park RJ, Jacob DJ, Li Q, Thiemens MH, Yantosca RM (2005) Sulfate formation in sea-salt aerosols: constraints from oxygen isotopes. J Geophys Res 110 (D10307). doi:10.1029/2004JD005659

Anguelova MD, Webster F (2006) Whitecap coverage from satellite measurements: a first step toward modeling the variability of oceanic whitecaps. J Geophys Res 111 (C3):C03017. doi:10.1029/2005JC003158

Ayash T, Gong S, Jia CQ (2008) Direct and indirect shortwave radiative effects of sea salt aerosols. J Clim 21 (13):3207-3220. doi:10.1175/2007JCLI2063.1

Bellouin N, Rae JGL, Jones A, Johnson CE, Haywood JM, Boucher O (2011) Aerosol forcing in the CMIP5 simulations by Hadgem2-ES and the role of ammonium nitrate. J Geophys Res. doi:10.1029/2011JD016074 (in press)

Berger AL (1978) Long-term variations of daily insolation and quaternary climatic changes. J Atmos Sci 35(12):2362–2367

Bigler M, Rothlisberger R, Lambert F, Stocker TF, Wagenbach D (2006) Aerosol deposited in East Antarctica over the last glacial cycle: detailed apportionment of continental and sea-salt contributions. J Geophys Res 111 (D08205). doi:10.1029/2005JD006469

Blanchard DC (1985) The oceanic production of atmospheric sea salt. J Geophys Res 90(Nc1):961–963

Braconnot P, Otto-Bliesner B, Harrison S, Joussaume S, Peterchmitt JY, Abe-Ouchi A, Crucifix M, Driesschaert E, Fichefet T, Hewitt CD, Kageyama M, Kitoh A, Laine A, Loutre MF, Marti O, Merkel U, Ramstein G, Valdes P, Weber SL, Yu Y, Zhao Y (2007) Results of PMIP2 coupled simulations of the Mid-Holocene and Last Glacial Maximum - Part 1: experiments and large-scale features. Clim Past 3(2):261–277

Briegleb BP (1992) Delta-Eddington approximation for solar radiation in the NCAR community climate model. J Geophys Res 97(D7):7603–7612

Carlson TN, Benjamin SG (1980) Radiative heating rates for saharan dust. J Atmos Sci 37(1):193–213

Carslaw KS, Boucher O, Spracklen DV, Mann GW, Rae JGL, Woodward S, Kulmala M (2010) A review of natural aerosol interactions and feedbacks within the earth system. Atmos Chem Phys 10:1701–1737. doi:10.5194/acp-10-1701-2010

Chin M, Ginoux P, Kinne S, Torres O, Holben BN, Duncan BN, Martin RV, Logan JA, Higurashi A, Nakajima T (2002) Tropospheric aerosol optical thickness from the GOCART model and comparisons with satellite and sun photometer measurements. J Atmos Sci 59(3):461–483

Christopher SA, Zhang JL (2002) Shortwave aerosol radiative forcing from MODIS and CERES observations over the oceans. Geophys Res Lett 29(18):1859. doi:10.1029/2002GL014803

CLIMAP project members (1981). Seasonal reconstructions of the earth's surface at the last glacial maximum, Geological Society of America Map and Chart Series MC-36

de Rooij WA, van der Stap CCAH (1984) Expansion of Mie scattering matrices in generalized spherical functions. Astron Astrophys 131:237–248

DeAngelis M, Steffensen JP, Legrand M, Clausen H, Hammer C (1997) Primary aerosol (sea salt and soil dust) deposited in Greenland ice during the last climatic cycle: comparison with east Antarctic records. J Geophys Res 102(C12):26681–26698

Dobbie S, Li JN, Harvey R, Chylek P (2003) Sea-salt optical properties and GCM forcing at solar wavelengths. Atmos Res 65(3–4):211–233

Easter RC, Ghan SJ, Zhang Y, Saylor RD, Chapman EG, Laulainen NS, Abdul-Razzak H, Leung LR, Bian X, Zaveri RA (2004) MIRAGE: model description and evaluation of aerosols and trace gases. J Geophys Res 109(D20):1–46. doi:10.1029/2004JD004571

Erickson DJ, Merrill JT, Duce RA (1986) Seasonal estimates of global atmospheric sea-salt distributions. J Geophys Res 91(D1):1067–1072

Forster P, Ramaswamy V, Artaxo P, Berntsen T, Betts R, Fahey DW, Haywood J, Lean J, Lowe DC, Myhre G, Nganga J, Prinn R, Raga G, Schulz M, Dorland RV (2007) Changes in atmospheric constituents and in radiative forcing. In: climate change 2007: the physical science basis. contribution of working group i to the fourth assessment report of the intergovernmental panel on climate change. Cambridge University Press, Cambridge and New York, NY pp 131–217

Galloway JN, Savoie DL, Keene WC, Prospero JM (1993) The temporal and spatial variability of scavening ratios for nss sulfate, nitrate, methanesulfonate and sodium in the atmosphere over the North Atlantic Ocean. Atmos Environ 27A(2):235–250

Gerber HE (1985) Relative humidity parameterization of the navy aerosol model (NAM). Navy Research Lab, Washington DC

Ginoux P, Horowitz LW, Ramaswamy V, Geogdzhayev IV, Holben BN, Stenchikov G, Tie X (2006) Evaluation of aerosol distribution and optical depth in the Geophysical Fluid Dynamics Laboratory coupled model CM2.1 for present climate. J Geophys Res 111(D22):D22210. doi:10.1029/2005JD006707

Gong SL (2003) A parameterization of sea-salt aerosol source function for sub- and super-micron particles. Global Biogeochem Cycles 17(4):1097. doi:10.1029/2003GB002079

Gong SL, Barrie LA, Prospero JM, Savoie DL, Ayers GP, Blanchet JP, Spacek L (1997) Modeling sea-salt aerosols in the atmosphere. 2. Atmospheric concentrations and fluxes. J Geophys Res 102(D3):3819–3830

Grini A, Myhre G, Sundet JK, Isaksen ISA (2002) Modeling the annual cycle of sea salt in the global 3D model Oslo CTM2:

concentrations, fluxes, and radiative impact. J Clim 15(13): 1717–1730
Guelle W, Schulz M, Balkanski Y, Dentener F (2001) Influence of the source formulation on modeling the atmospheric global distribution of sea salt aerosol. J Geophys Res 106(D21):27509–27524
Hansen J, Lacis A, Rind D, Russell G, Stone P, Fung I, Ruedy R, Lerner J (1984) Climate sensitivity: analysis of feedback mechanisms. In: climate processes and climate sensitivity. Geophysical monograph 29. AGU, Washington, DC, pp 130–163
Haxeltine A, Prentice IC (1996) BIOME3: an equilibrium terrestrial biosphere model based on ecophysiological constraints, resource availability, and competition among plant functional types. Global Biogeochem Cycles 10(4):693–709
Haywood JM, Ramaswamy V, Soden BJ (1999) Tropospheric aerosol climate forcing in clear-sky satellite observations over the oceans. Science 283(5406):1299–1303. doi:10.1126/science.283.5406.1299
Hess M, Koepke P, Schult I (1998) Optical properties of aerosols and clouds: the software package OPAC. Bull Am Meteorol Soc 79(5):831–844
Holben BN, Eck TF, Slutsker I, Tanre D, Buis JP, Setzer A, Vermote E, Reagan JA, Kaufman YJ, Nakajima T, Lavenu F, Jankowiak I, Smirnov A (1998) AERONET—a federated instrument network and data archive for aerosol characterization. Remote Sens Environ 66(1):1–16
Irshad R, Grainger RG, Peters DM, McPheat RA, Smith KM, Thomas G (2009) Laboratory measurements of the optical properties of sea salt aerosol. Atmos Chem Phys 9(1):221–230
Jacobson MZ (2001) Global direct radiative forcing due to multicomponent anthropogenic and natural aerosols. J Geophys Res 106(D2):1551–1568
Jaegle L, Quinn PK, Bates TS, Alexander B, Lin J-T (2011) Global distribution of sea salt aerosols: new constraints from in situ and remote sensing observations. Atmos Chem Phys 11:3137–3157. doi:10.5194/acp-11-3137-2011
Jansen E, Overpeck J, Briffa KR, Duplessy J-C, Joos F, Masson-Delmotte V, Olago D, Otto-Bliesner B, Peltier WR, Rahmstorf S, Ramesh R, Raynaud D, Rind D, Solomina O, Villalba R, Zhang De (2007) Palaeoclimate. In: Jouzel J, Mitchell J (eds) Climate change 2007: the physical science basis. Contribution of working group i to the fourth assessment report of the intergovernmental panel on climate change. Cambridge University Press, Cambridge and New York, NY, pp 433–497
Jiang D (2008) Vegetation and soil feedbacks at the last glacial maximum. Palaeogeogr Palaeoclimatol Palaeoecol 268:39–46
Kalnay E, Kanamitsu M, Kistler R, Collins W, Deaven D, Gandin L, Iredell M, Saha S, White G, Woollen J, Zhu Y, Leetmaa A, Reynolds B, Chelliah M, Ebisuzaki W, Higgins W, Janowiak J, Mo KC, Ropelewski C, Wang J, Jenne R, Joseph D (1996) The NCEP/NCAR 40-year reanalysis project. Bull Amer Meteor Soc 77(3):437–471
Kaufman YJIK, Remer LA, Rosenfeld D, Rudich Y (2005) The effect of smoke, dust and pollution aerosol on shallow cloud development over the Atlantic Ocean. Proc Natl Acad Sci 102(32): 11207–11212. doi:10.1073/pnas.0505191102
Kiehl JT, Briegleb BP (1991) A new parameterization of the absorptance due to the 15 μm band system of carbon dioxide. J Geophys Res 96(D5):9013–9019
Koch D, Schmidt GA, Field CV (2006) Sulfur, sea salt, and radionuclide aerosols in GISS ModelE. J Geophys Res 111(D6): D06206. doi:10.1029/2004JD005550
Levitus S, Antonov JI, Boyer TP, Stephens C (2000) Warming of the world ocean. Science 287:2225–2229
Li J, Ma X, von Salzen K, Dobbie S (2008) Parameterization of sea-salt optical properties and physics of the associated radiative forcing. Atmos Chem Phys 8(16):4787–4798
Liang X (1996) Description of a nine-level grid point atmospheric general circulation model. Adv Atmos Sci 13(3):269–298
Liao H, Seinfeld JH, Adams PJ, Mickley LJ (2004) Global radiative forcing of coupled tropospheric ozone and aerosols in a unified general circulation model. J Geophys Res 109:D16207. doi: 10.1029/2003JD004456
Liao H, Henze DK, Seinfeld JH, Wu SL, Mickley LJ (2007) Biogenic secondary organic aerosol over the United States: comparison of climatological simulations with observations. J Geophys Res 112(D6):D06201. doi:10.1029/2006JD007813
Loeb NG, Manalo-Smith N (2005) Top-of-atmosphere direct radiative effect of aerosols over global oceans from merged CERES and MODIS observations. J Clim 18(17):3506–3526. doi:10.1175/JCLI3504.1
Lubin D, Satheesh SK, McFarquar G, Heymsfield AJ (2002) Longwave radiative forcing of Indian Ocean tropospheric aerosol. J Geophys Res 107(D19):8004. doi:10.1029/2001JD001183
Ma X, von Salzen K, Li J (2008) Modelling sea salt aerosol and its direct and indirect effects on climate. Atmos Chem Phys 8(5):1311–1327
Mahowald NM, Lamarque JF, Tie XX, Wolff E (2006a) Sea-salt aerosol response to climate change: last glacial maximum, preindustrial, and doubled carbon dioxide climates. J Geophys Res 111(D5):D05303. doi:10.1029/2005JD006459
Mahowald NM, Yoshioka M, Collins WD, Conley AJ, Fillmore DW, Coleman DB (2006b) Climate response and radiative forcing from mineral aerosols during the last glacial maximum, pre-industrial, current and doubled-carbon dioxide climates. Geophys Res Lett 33(20):L20705. doi:10.1029/2006GL026126
Manabe S, Broccoli AJ (1985) The Influence of continental ice sheets on the climate of an ice age. J Geophys Res 90(D1):2167–2190
Mishchenko MI, Dlugach JM, Yanovitskij EG, Zakharova NT (1999) Bidirectional reflectance of flat, optically thick particulate layers: an efficient radiative transfer solution and applications to snow and soil surfaces. J Quant Spectrosc Radiat Transf 63:409–432
Monahan EC, Spiel DE, Davidson KL (1986) A model of marine aerosol generation via whitecaps and wave disruption. In: Monahan EC, Niocaill GM (eds) Oceanic whitecaps and their role in air-sea exchange processes. Kluwer Academic, Dordrecht, pp 167–174
Mulcahy JP, O'Dowd CD, Jennings SG, Ceburnis D (2008) Significant enhancement of aerosol optical depth in marine air under high wind conditions. Geophys Res Lett 35(16):L16810. doi: 10.1029/2008GL034303
Myhre G, Bellouin N, Berglen T, Berntsen T, Boucher O, Grini A, Isaksen I, Johnsrud M, Mishchenko M, Stordal F, Tanré D (2007) Comparison of the radiative properties and direct radiative effect of aerosols from a global aerosol model and remote sensing data over ocean. Tellus 59B:115–129. doi: 10.1111/j.1600-0889.2006.00226.x
Myhre G, Berglen TF, Johnsrud M, Hoyle CR, Berntsen TK, Christopher SA, Fahey DW, Isaksen ISA, Jones TA, Kahn RA, Loeb N, Quinn P, Remer L, Schwarz JP, Yttri KE (2009) Modelled radiative forcing of the direct aerosol effect with multi-observation evaluation. Atmos Chem Phys 9:1365–1392. doi:10.5194/acp-9-1365-2009
Peltier WR (2004) Global glacial isostasy and the surface of the ice-age earth: The ice-5G (VM2) model and grace. Annu Rev Earth Planet Sci 32:111–149
Petit JR, Briat M, Royer A (1981) Ice-age aerosol content from East Antarctic ice core samples and past wind strength. Nature 293(5831):391–394. doi:10.1038/293391a0
Petit JR, Mounier L, Jouzel J, Korotkevich YS, Kotlyakov VI, Lorius C (1990) Palaeoclimatological and chronological implications of the Vostok core dust record. Nature 343(6253):56–58

Petit JR, Jouzel J, Raynaud D, Barkov NI, Barnola J-M, Basile I, Bender M, Chappellaz J, Davis M, Delaygue G, Delmotte M, Kotlyakov VM, Legrand M, Lipenkov VY, Lorius C, PÉpin L, Ritz C, Saltzman E, Stievenard M (1999) Climate and atmospheric history of the past 420,000 years from the Vostok ice core, Antarctica. Nature 399:429–436. doi:10.1038/20859

Prospero JM (1996) The atmospheric transport of particles to the Ocean. In: Ittekkot V, Schäfer P, Honjo S, Depetris PJ (eds) Particle flux in the ocean, SCOPE, vol 57. Wiley, Chichester, pp 19–52

Rankin AM, Wolff EW, Martin S (2002) Frost flowers: implications for tropospheric chemistry and ice core interpretation. J Geophys Res 107(D23):4683. doi:10.1029/2002JD002492

Reader MC, McFarlane N (2003) Sea-salt aerosol distribution during the last glacial maximum and its implications for mineral dust. J Geophys Res 108(D8):4253. doi:10.1029/2002JD002063

Reddy MS, Boucher O, Balkanski Y, Schulz M (2005a) Aerosol optical depths and direct radiative perturbations by species and source type. Geophys Res Lett 32(12):L12803. doi:10.1029/2004GL021743

Reddy MS, Boucher O, Bellouin N, Schulz M, Balkanski M, Dufresne Y, Pham M (2005b) Estimates of global multicomponent aerosol optical depth and direct radiative perturbation in the Laboratoire de Meteorologie Dynamique general circulation model. Geophys Res Lett 110(D10):D10S16. doi:10.1029/2004JD004757

Remer LA, Kaufman YJ (2006) Aerosol direct radiative effect at the top of the atmosphere over cloud free ocean derived from four years of MODIS data. Atmos Chem Phys 6:237–253. doi:10.5194/acp-6-237-2006

Rothlisberger R, Mulvaney R, Wolff EW, Hutterli MA, Bigler M, Sommer S, Jouzel J (2002) Dust and sea salt variability in central East Antarctica (Dome C) over the last 45 kyrs and its implications for southern high-latitude climate. Geophys Res Lett 29(20):1963. doi:10.1029/2002gl015186

Satheesh SK, Lubin D (2003) Short wave versus long wave radiative forcing by Indian Ocean aerosols: role of sea-surface winds. Geophys Res Lett 30(13):1695. doi:10.1029/2003GL017499

Smith MH, Park PM, Consterdine IE (1993) Marine aerosol concentration and estimated fluxes over sea. Quart J Roy Meteor Soc 119:809–824

Takemura T, Okamoto H, Maruyama Y, Numaguti A, Higurashi A, Nakajima T (2000) Global three-dimensional simulation of aerosol optical thickness distribution of various origins. J Geophys Res 105(D14):17853–17873

Takemura T, Nakajima T, Dubovik O, Holben BN, Kinne S (2002) Single-scattering albedo and radiative forcing of various aerosol species with a global three-dimensional model. J Clim 15(4):333–352

Tang IN, Tridico AC, Fung KH (1997) Thermodynamic and optical properties of sea salt aerosols. J Geophys Res 102(D19):23269–23275

Tegen I, Hollrig P, Chin M, Fung I, Jacob D, Penner J (1997) Contribution of different aerosol species to the global aerosol extinction optical thickness: estimates from model results. J Geophys Res 102(D20):23895–23916

Textor C, Schulz M, Guibert S, Kinne S, Balkanski Y, Bauer S, Berntsen T, Berglen T, Boucher O, Chin M, Dentener F, Diehl T, Easter R, Feichter H, Fillmore D, Ghan S, Ginoux P, Gong S, Kristjansson JE, Krol M, Lauer A, Lamarque JF, Liu X, Montanaro V, Myhre G, Penner J, Pitari G, Reddy S, Seland O, Stier P, Takemura T, Tie X (2006) Analysis and quantification of the diversities of aerosol life cycles within AeroCom. Atmos Chem Phys 6:1777–1813

Tie XX, Madronich S, Walters S, Edwards DP, Ginoux P, Mahowald N, Zhang RY, Lou C, Brasseur G (2005) Assessment of the global impact of aerosols on tropospheric oxidants. J Geophys Res 110(D3):D03204. doi:10.1029/2004JD005359

Wagenbach D, Ducroz F, Mulvaney R, Keck L, Minikin A, Legrand M, Hall JS, Wolff EW (1998) Sea-salt aerosol in coastal Antarctic regions. J Geophys Res 103(D9):10961–10974

Woodward S (2001) Modeling the atmospheric life cycle and radiative impact of mineral dust in the Hadley Centre climate model. J Geophys Res 106(D16):18155–18166

Yu H, Dickinson RE, Chin M, Kaufman YJ, Zhou M, Zhou L, Tian Y, Dubovik O, Holben BN (2004) Direct radiative effect of aerosols as determined from a combination of MODIS retrievals and GOCART simulations. J Geophys Res 109 (D03206). doi:10.1029/2003JD003914

Yue X, Wang HJ (2009) The application of the CCM3/NCAR radiation scheme in IAP-AGCM. Chin J Atmos Sci 33(1):16–28

Yue X, Wang HJ, Wang Z, Fan K (2009) Simulation of dust aerosol radiative feedback using the global transport model of dust: 1. Dust cycle and validation. J Geophys Res 114:D10202. doi:10.1029/2008JD010995

Yue X, Wang HJ, Liao H, Fan K (2010) Simulation of dust aerosol radiative feedback using the GMOD: 2. Dust-climate interactions. J Geophys Res 115:D04201. doi:10.1029/2009JD012063

Yue X, Wang HJ, Liao H, Jiang DB (2011) Simulation of the direct radiative effect of mineral dust aerosol on the climate at the last glacial maximum. J Clim 24(3):843–858. doi:10.1175/2010JCLI3827.1

Zeng Q, Zhang X, Liang X, Yuan C, Chen SF (1989) Documentation of IAP two-level atmospheric general circulation model. DOE/ER/60314-H1, CDIAC TR044. Dept. of Energy, Washington, DC

Zhang X (1990) Dynamical framework of IAP nine-level atmospheric general circulation model. Adv Atmos Sci 7(1):67–77

Zhao TX-P, Yu H, Laszlob I, Chinc M, Conant WC (2008) Derivation of component aerosol direct radiative forcing at the top of atmosphere for clear-sky oceans. J Quant Spectrosc Radiat Transf 109:1162–1186. doi:10.1016/j.jqsrt.2007.10.006